# TOWARD ORBITAL SEISMOLOGY: THEORY FOR SPECKLE NOISE REDUCTION IN LASER DOPPLER VIBROMETER MEASUREMENTS ON DISTANT ROUGH SURFACES

by

Samuel W. Courville

**© Copyright by Samuel W. Courville, 2019**

All Rights Reserved

A thesis submitted to the Faculty and the Board of Trustees of the Colorado School of Mines in partial fulfillment of the requirements for the degree of Master of Science (Geophysics).

Golden, Colorado

Date _____

Signed: _____
Samuel W. Courville

Signed: _____
Dr. Paul C. Sava
Thesis Advisor

Golden, Colorado

Date _____

Signed: _____
Dr. Paul C. Sava
Professor and Head
Department of Geophysics

# ABSTRACT

The interior structures of small planetary bodies such as asteroids and comets are an enigma, yet understanding them has immense value. Knowing the internal structure is important for understanding the formation and evolution of the solar system and also has implications for in-situ resource exploitation and planetary defense from asteroids. Despite the immense value, no detailed investigation of the interior properties of an asteroid has yet been made. Although orbital radar and lander based seismological approaches have been proposed to make direct interior observations, it has not yet been demonstrated that radar could transmit through a rocky asteroid, nor that landing multiple seismometers is feasible or affordable. An elegant alternative to landed seismometers is orbital laser Doppler vibrometry, which could record seismic shaking of a small body without contact with the surface. Laser Doppler vibrometers (LDVs) are mature instruments for terrestrial applications; and could function similarly in a space environment. However, when incident on a rough surface like an asteroid regolith, an LDV is subject to laser speckle noise which may be misinterpreted as seismic shaking. I address the challenge of making LDV measurements on naturally rough surfaces by quantifying the laser speckle noise that an orbital LDV would encounter during a hypothetical orbital measurement. Specifically, I simulate an LDV measurement of a seismic signal generated by an impact source on the asteroid 101955 Bennu. I demonstrate that speckle noise can be attenuated by combining multiple signals recorded by an orbital seismometer equipped with multiple LDV sensors. By mitigating laser speckle, I demonstrate that an orbital LDV can record seismic signals on a natural asteroid surface, which would enable an orbital seismometer to achieve the dense global coverage necessary for high resolution interior imaging.

TABLE OF CONTENTS

ABSTRACT . . . . . iii

LIST OF FIGURES . . . . . vi

LIST OF ABBREVIATIONS . . . . . x

ACKNOWLEDGMENTS . . . . . xi

DEDICATION . . . . . xii

CHAPTER 1 INTRODUCTION . . . . . 1

CHAPTER 2 SPECKLE NOISE ATTENUATION IN ORBITAL LASER VIBROMETER SEISMOLOGY . . . . . 10

2.1 Introduction . . . . . 11

2.2 LDV speckle noise simulation . . . . . 15

2.2.1 LDV theory . . . . . 15

2.2.2 Laser speckle patterns . . . . . 17

2.2.3 Speckle induced measurement error . . . . . 26

2.2.4 Speckle noise reduction . . . . . 28

2.3 Impact seismic signal simulation . . . . . 30

2.3.1 Impact source . . . . . 30

2.3.2 Seismic propagation through 101955 Bennu . . . . . 35

2.4 Seismic signal separation from speckle noise . . . . . 41

2.4.1 Signal diversity . . . . . 41

2.4.2 Maximal ratio combining . . . . . 42

2.4.3 Signal fitting model . . . . . 44
2.5 Discussion . . . . . 47
2.6 Conclusion . . . . . 53
2.7 Acknowledgments . . . . . 53
CHAPTER 3 CONCLUSIONS . . . . . 55
3.1 Future work . . . . . 56
REFERENCES CITED . . . . . 60

LIST OF FIGURES

Figure 1.1 Asteroids and comets of the solar system that have been visited by spacecraft to date. Montage by Emily Lakdawalla, planetary.org. Data from NASA / Jet Propulsion Laboratory / Johns Hopkins University Applied Physics Laboratory / University of Maryland / JAXA / ESA / OSIRIS team / Russian Academy of Sciences / China National Space Agency. . . . . 2

Figure 1.2 This thesis analyzes the noise that arises from transverse motion by an LDV over a rough surface, where the laser beam translates over the vibrating surface. The noise trace in Figure 1.3 is generated by acquiring data using this acquisition setup. . . . . 6

Figure 1.3 An LDV records two parameters as a function of time, (top) the intensity of reflected light off the target surface, and (bottom) the velocity component of the target in parallel with the LDV's laser beam. This figure shows a laboratory measurement of a motionless sample of asteroid regolith simulant while the LDV moves 10 cm/s translationally relative to the sample (no velocity in the direction of the beam). The LDV should record zero velocity, but instead records noise caused by the laser spot moving over the sample's rough surface. Significant noise is present in both the intensity and velocity signal. . . . . 7

Figure 1.4 Asteroid 101955 Bennu: the hypothetical target of this thesis work. Credit: NASA/Goddard/University of Arizona. . . . . 9

Figure 2.1 The seismic data acquisition scenario. We simulate an LDV orbiting with a velocity of 2.5 cm/s at a distance of 2 km from the surface of 0.5 km wide asteroid 101955 Bennu. The impactor weighs 2 kg and travels at 2 km/s upon impact with the surface. . . . . 16

Figure 2.2 A schematic of a Laser Doppler Vibrometer (LDV). The original laser beam is split into a measurement and reference beam at the first beam splitter (BS1). The measurement beam is directed at a vibrating target. In-line motion of the target Doppler shifts the frequency of the reflected beam. Upon return, the reflected beam is redirected by BS2 toward the detector. BS3 combines the reflected and reference beams. Due to the frequency shift of the reflected beam, the combined beams produce time dependent interference (optical heterodyning), which contains information about the surface motion (Equation 2.2) . . . . . 18

Figure 2.3 Illustration of how a coherent laser beam is reflected as an incoherent speckle pattern if the surface is rough. Not to scale; the beam and speckle sizes are exaggerated. . . . . 19

Figure 2.4 Illustration of speckle pattern computation from a rough surface (not to scale). Each surface tile contributes to the electric field recorded at the detector plane. The detector plane is 2 km above the rough surface. The red circle indicates the area of the LDV detector. The black circle with diameter $w$ indicates the $1/e^2$ Gaussian beam footprint. . . . . 23

Figure 2.5 Panels (a), (b), and (c) show random rough surfaces with peak relief of $10^{-7}$, $10^{-6}$, and $10^{-5}$ meters, respectively. Panels (d), (e), and (f), display the reflected light recorded at a detector 2 km away for the corresponding surfaces (a), (b), and (c). The simulated laser has a Gaussian beam profile with a $1/e^2$ radius of 2.5 cm, and a wavelength of 775 nm. When the surface roughness is less than wavelength (a), the surface acts as a mirror, and the beam profile is simply reflected (d). When the surface roughness is on the same order of magnitude as the laser wavelength (b), the reflected light has a bright center and a faint interference speckle pattern around it (e). For roughness much greater than the wavelength (c), a full speckle interference pattern develops (f). . 24

Figure 2.6 Illustration of the property that speckle patterns are independent of the lateral roughness scale. The speckle pattern (d) from a rough surface with grains that are approximately 0.5 mm across (a) is statistically indistinct from speckle patterns (e) and (f), which were produced by grains that are 1 mm (b) or 5 mm across (c). . . . . 25

Figure 2.7 (a) An example of rough topography (map and profile view) with multiple different scales of roughness. We simulate an LDV velocity measurement from a distance of 2 km as the laser spot moves across the map from left to right at a velocity of 5 cm/sec. The red circle on the map view indicates the $1/e^2$ radius of the Gaussian laser spot. The surface is motionless. (b) Erroneous LDV velocity measurement from surface roughness induced speckle noise. . . . . 27

Figure 2.8 Speckle patterns for the case when the laser spot moves across a rough surface at 5 cm /sec. The red circle indicates the detector size. $t_1$, $t_2$, and $t_3$ correspond to times when the detector records a dark, medium, and bright portion of the speckle pattern. . . . . 28

Figure 2.9 (a) Illustration of LDV intensity recorded as a function of time, (b) the relative phase as a function of time, (c) and the erroneous velocity recorded by the LDV due to the variable phase. The dashed lines correspond to $t_1$, $t_2$, and $t_3$ in the speckle images in Figure 2.8. The velocity signal has peaks when the phase changes quickly; the phase changes the quickest when the signal intensity is low. . . . . 29

Figure 2.10 Each different color curve corresponds to a realization of LDV speckle noise from an orbital LDV placed at 2 km from the surface and orbiting at 5 cm/s as depicted in Figure 2.1. . . . . 30

Figure 2.11 Simulated RMS velocity noise as a function of orbital velocity for an LDV positioned 2 km from an asteroid surface. The LDV has a 775 nm laser with a $1/e^2$ spot radius of 2.5 cm. The speckle noise is larger if the beam translates over the asteroid surface (red) than in the case where the beam rotates about a fixed point on the surface (blue). . . . . 31

Figure 2.12 (a) The ground motion signals from an impact seismic source similar to the Hayabusa2 SCI after propagating 500 m in a 450 m/s velocity homogeneous model. The examples shown correspond to high efficiency $k = 10^{-3}$ and low efficiency $k = 10^{-5}$ impacts. (b) Illustrates the frequency spectrum of the seismic signals. . . . . 34

Figure 2.13 Rubble pile asteroid velocity model we use to simulate seismic signals. . 35

Figure 2.14 Wavefield snapshots from an impactor with an efficiency of $10^{-5}$ at $t = 0.15$ s, $t = 0.45$ s, $t = 0.75$ s, and $t = 1.05$ s after impact, respectively. The blue dot indicates the impact location, and the red dot indicates the LDV recording location. . . . . 36

Figure 2.15 Wavefield snapshots from an impactor with an efficiency of $10^{-3}$ at at $t = 0.15$ s, $t = 0.45$ s, $t = 0.75$ s, and $t = 1.05$ s after impact respectively. The blue dot indicates the impact location, and the red dot indicates the LDV recording location. . . . . 37

Figure 2.16 Comparison of a speckle noise trace from Figure 2.10 with a seismic trace from an impactor with an efficiency of $k = 10^{-3}$. . . . . 38

Figure 2.17 Comparison of a speckle noise trace from Figure 2.10 with a seismic trace from an impactor with an efficiency of $k = 10^{-5}$. Unlike the high seismic efficiency impact signal in Figure 2.16, the lower seismic efficiency impact produces a seismic signal with much lower amplitude than the speckle noise. . . . . 39

Figure 2.18 LDV detector arrangements capable of recording multiple signals: (a) represents 1 detector recording 2 signals of orthogonal polarization, (b) 3 detectors recording 6 signals, and (c) 7 detectors recording 14 signals. Each detector is roughly the same size as the speckles in order to record independent speckle noise. . . . . 47

Figure 2.19 Signal-to-noise ratio of the approximation of the seismic trace in Figure 2.17 as a function of DPSS subspace bandwidth. The band is centered at 30 Hz, so a bandwidth of 15 Hz corresponds to a DPSS subspace that spans 15-45 Hz. The seismic signal can be well approximated using a narrow bandwidth. . . . . 48

Figure 2.20 Recovered signal after combining multiple data traces that contain the same seismic signal and similar speckle noise as in Figure 2.17. (a) One LDV signal without any filtering; (b) combination two signals; (c) combination of six signals; (d) combination of 14 signals. Combining multiple signals significantly reduces speckle noise. . . . . 49

Figure 2.21 Signal improvement as a function of the number of signals combined. Each curve indicates the average of 20 simulations, and the uncertainty bars represent the standard deviation of the simulations. Black illustrates the weighted average approach, yellow illustrates the case using a narrow band to approximate the signal; magenta illustrates the case using a wide band for approximation, and cyan demonstrates a case using an optimal frequency band. . . . . 50

Figure 2.22 Signal recovery as a function of the peak ground velocity of the seismic signal. The signal used for testing is the same as shown in Figure 2.17, but scaled by different peak ground velocities ranging from $10^{-5}$ to $10^{-8}$ m/s. The dots indicate separation with a DPSS fit within 7 to 53 Hz, and the lines indicate separation with the weighted average approach. Red represents the SNR from 1 receiver, green the SNR after combining 2 signals, yellow the SNR after combining 6 signals, and blue, the SNR after combining 14 signals. The black line indicates the optimal signal approximation using the chosen bandwidth. . . . . 51

# LIST OF ABBREVIATIONS

COmet Nucleus Sounding Experiment by Radiowave Transmission . . . . . CONSERT

Center for Wave Phenomena . . . . . CWP

Discrete Prolate Spheroidal Sequences . . . . . DPSS

European Space Administration . . . . . ESA

Japan Aerospace Exploration Agency . . . . . JAXA

Laser Doppler Vibrometer . . . . . LDV

Maximal Ratio Combining . . . . . MRC

National Aeronautics and Space Administration . . . . . NASA

Origins, Spectral Interpretation, Resource Identification, Security, Regolith Explorer . . . . . OSIRIS-REx

Peak Ground Velocity . . . . . PGV

Root Mean Square . . . . . RMS

Hayabusa2 Small Carry-on Impactor . . . . . SCI

Signal-to-Noise Ratio . . . . . SNR

# ACKNOWLEDGMENTS

Two years ago, I graduated as a bright eyed geophysics student looking to become involved in planetary geophysics research. My ultimate goal: help design new spacecraft that could explore the solar system and help us learn more about the origins of our world, life, and ourselves. I am forever grateful to Dr. Paul Sava for giving me the opportunity to help design an innovative instrument to accomplish just that. His guidance will forever grant me the skills I need to be a successful researcher in my future endeavors.

Over the course of researching for this thesis, I received teaching and assistance from many professors. I am grateful to Dr. Mike Wakin for his patient help in explaining signal processing and separation theory to me. My thesis would not be complete without his insight. Additionally, I thank Dr. Charles Durfee for teaching me the fundamentals of laser physics. If you read this, I profusely apologize for breaking one of your lasers. I appreciate the professional development advice I received from Dr. Roel Snieder. I also thank Dr. Erik Asphaug for providing occasional and valuable sanity checks on my work. Last, but certainly not least, I am indebted to the guidance provided by my committee members. From Dr. Chris Dreyer I learned much about spacecraft design and mission architecture, and from Dr. Ebru Bozdag, I learned the fundamentals of seismology.

None of my work would have been possible without the support of my friends and colleagues. I thank Hayden Powers, Thomas Rapstine, Ivan Lim Chen Ning, Iga Pawelec, Odette Aragao, and Colton Kohnke for providing support whenever I needed it. I also could not have graduated without the invaluable departmental assistance of Michelle Szobody, Dianne Witters, Dawn Umpleby, and Debra Marrufo.

Finally, I owe the most to my parents, my big brother, my little sister, and my significant other. For without their unconditional encouragement, care, and support, I would not have succeeded.

For my family

# CHAPTER 1

# INTRODUCTION

Approximately 66 million years ago, a colossal 10-80 km wide asteroid collided with Earth. The catastrophic Chicxulub impact triggered a mass extinction, which doomed the dinosaurs (Renne et al., 2013). Although colossal impacts are rare, they possess a significant hazard to all life on Earth. In 1908, a smaller 50-190 m diameter asteroid collided with Earth and exploded mid-air over a remote location near the Tunguska river in Siberia. The air burst from the Tunguska event leveled 2,000 $km^2$ of forest (Jenniskens et al., 2019). Had it exploded in a more populous region, its devastation would have been much more catastrophic. Such an event occurred in 2013, when an asteroid exploded over the city of Chelyabinsk, Russia. Although the asteroid was only about 20 m in diameter, the resulting air burst caused multiple injuries and extensive damage to over a wide area (Kartashova et al., 2018). Such events remind us that the threat of asteroid impacts is real, and the possibility of catastrophic impacts in the future cannot be ignored.

Survey networks and early warning telescopes provide the ability to detect potentially hazardous asteroids before they collide with Earth (Tonry et al., 2018). Yet, if we did detect an asteroid on a collision course, what would we do? How would we stop it? Frighteningly, we do not know yet. Several proposals exist (Cheng et al., 2015, 2012; Kueppers et al., 2015), but all are preconditioned on one unknown factor of asteroids: their internal strength. How well do they hold together? Could a ballistic impact or explosive device disrupt an asteroid significantly enough to prevent it from colliding with Earth? Could a spacecraft designed to push an asteroid do so while the asteroid stays together in one piece? These questions come down to understanding the interior properties of asteroids.

Aside from mitigating potential human annihilation, understanding the internal structure of asteroids and comets is also scientifically important. Determining the internal structure

of small bodies allows us to infer the formation environment and early evolution of the solar system (Asphaug, 2009). The interiors can also tell us how planets, like our own, originally accreted (Asphaug, 2009). With each small body visited, a new and unique world is discovered (Figure 1.1). It is likely that comet and asteroid interiors are equally diverse. Comets could perhaps have weakly layered structure, as they periodically outgas during close passings of the Sun (Massironi et al., 2015). Small asteroids could be little more than fluffy balls of regolith, or piles of rubble (Asphaug et al., 2002). Larger asteroids like Eros, and small moons like Phobos, could be fractured monoliths (Asphaug, 2009). It is likely that each asteroid and comet has a different story to tell, and a method to uncover these stories with observations from spacecraft is highly desirable.

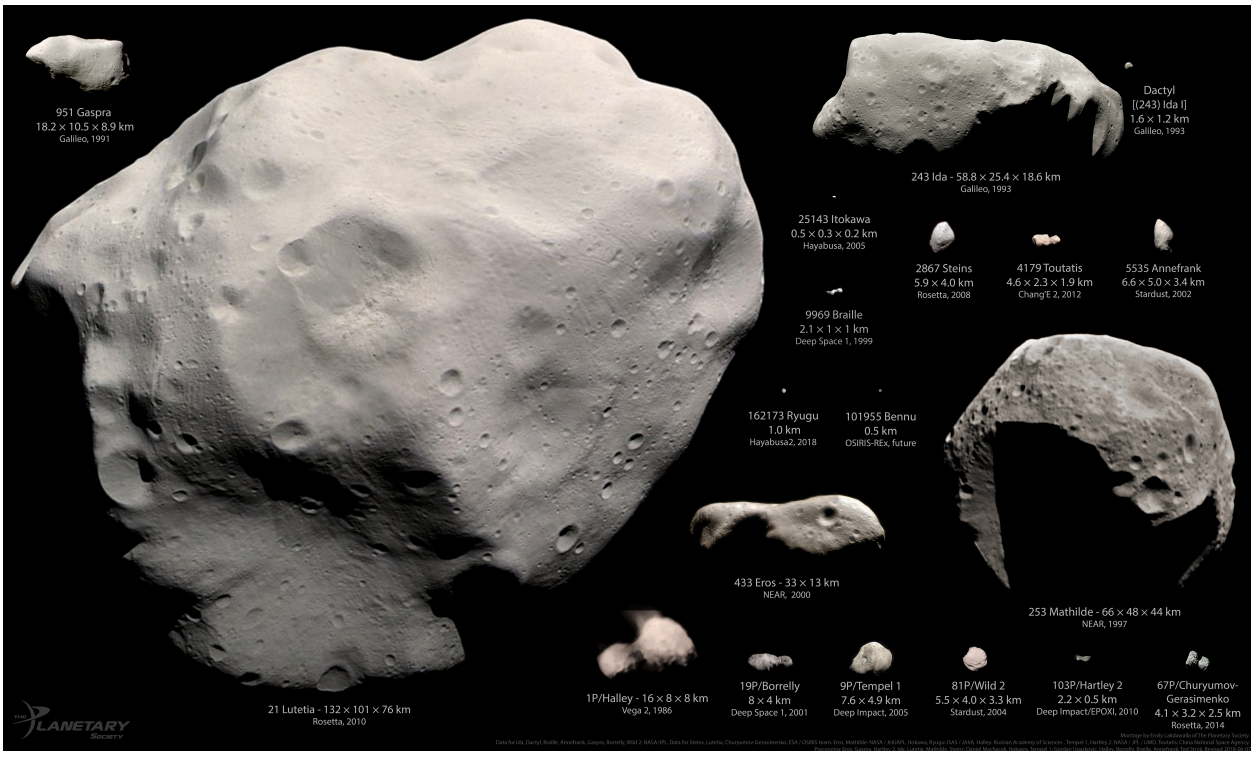


Figure 1.1: Asteroids and comets of the solar system that have been visited by spacecraft to date. Montage by Emily Lakdawalla, planetary.org. Data from NASA / Jet Propulsion Laboratory / Johns Hopkins University Applied Physics Laboratory / University of Maryland / JAXA / ESA / OSIRIS team / Russian Academy of Sciences / China National Space Agency.

Complicated theoretical frameworks have been developed to infer the internal structure of asteroids from surface topography and morphology. For example, the presence of cratering implies bulk strength, and the lack-thereof implies that impacts could shake loosely bound material and trigger global resurfacing events (Asphaug, 2008; Richardson et al., 2005). The most direct observations that are currently available of small body interior structure are bulk density measurements derived from gravity data. For example, the asteroid 101955 Bennu must be 60% empty space in order to explain its low density as determined from gravity measurements (Scheeres et al., 2015). Yet, it is not understood how this void space manifests. Thus, current observations have raised more questions about internal structure than answers. The majority of internal structure hypotheses remain to be robustly tested with direct measurements.

How do we directly measure the interior properties of an asteroid or comet? The two most promising methods are radar sounding and seismology. The partially successful COmet Nucleus Sounding Experiment by Radiowave Transmission (CONSERT) on ESA's Rosetta mission demonstrated that radar waves can travel through comets (Ciarletti et al., 2017). However, the comet appeared to be homogeneous to radar waves. Radar waves in contrast to seismic waves are sensitive to electromagnetic properties, which may or may not be correlated with geologic structure or strength. Additionally, radar waves may penetrate through icy comet material, but could attenuate quickly in a more rocky body like an asteroid (Grimm et al., 2015).

Measuring seismic waves that travel through the interior of an asteroid, the topic of this thesis, is a desirable alternative to radar imaging. In contrast to radar waves, seismic waves are dependent on the strength properties of the medium with which they travel through. Additionally, if a spacecraft could take multiple recordings of seismic waves that pass through the core with different paths, an image of the internal structure could be made like an MRI scan (Sava and Asphaug, 2019). Unfortunately, recording seismic waves on an asteroid is challenging. To record seismic data conventionally, a spacecraft would need to land on the

surface, couple with the surface, and record precise motion as it moved with the surface. To achieve global coverage over an asteroid, a mission would need multiple landers scattered over the surface. Several have proposed mission concepts to accomplish seismic measurements, but the systems are undesirably complex, and prohibitively expensive (Huebner, 2004; Plescia et al., 2018; Walker et al., 2006). The technical difficulty of making seismic measurements provides a large barrier to overcome.

In order to overcome this barrier to measurement, Sava and Asphaug (2019) propose a paradigm shift for small body interior science: an orbital seismometer. Instead of requiring a lander to record seismic waves that have propagated through the interior of an asteroid, the measurement could be taken remotely from orbit. Because the instrument orbits around the asteroid, it could make measurements at many locations across the surface. This means that if there was a repeatable seismic source, over time, the instrument could collect global seismic data allowing for an image of the interior to be created. To achieve a remote sensing seismometer, the concept employs a laser Doppler vibrometer (LDV). Similar to a police radar gun, an LDV measures the Doppler shift of reflected light as a function of the target surface's motion. Specifically, an LDV shines a laser beam onto a target and records two things: the velocity of the target in-line with the laser beam, and the reflectivity of surface based on how much laser light is reflected.

Laser Doppler vibrometers are a well developed instrument. They are frequently used on Earth for a variety of remote vibration sensing purposes (Rothberg et al., 2017). However, they are typically operated in a laboratory environment, or on prepared surfaces (e.g. using retroreflective tape). To be effective on an asteroid in the concept proposed by Sava and Asphaug (2019), an LDV must be able to operate on an unprepared natural asteroid surface. If the orbital LDV requires landing laser retroreflectors, then an LDV becomes only marginally more convenient than landing conventional seismometers. Sava and Asphaug (2019) assume that an LDV can record accurate measurements on a natural asteroid surface. The primary goal of my thesis is to test this hypothesis and to design methods that address technical

challenges associated with LDV use on natural rough surfaces.

Like any good research project, my work began with a routine laboratory experiment gone wrong. The experiment was simple, take a sample of asteroid simulant (blended rocks designed to mimic the properties of asteroid regolith to the best of our knowledge), vibrate the sample, and record its motion with an off-the-shelf LDV. Since an LDV orbiting an asteroid would have its laser spot slowly translate across the asteroid's surface, I tested recording vibrations with an LDV in motion (Figure 1.2). I found that recordings from an LDV in motion exhibited significant noise (Figure 1.3). I had rediscovered the hard way a well known challenge for LDV measurements on rough surfaces: speckle noise. Extensive research by others have found that LDVs are susceptible to laser speckle noise when the laser spot moves along a rough surface (Rothberg et al., 2004). Speckle noise, as introduced in Chapter 2.2, is a result of monochromatic light interference from a rough surface. Essentially, the roughness of natural surfaces distorts the reflected laser wavefront and obscures the signal of the ground motion. Speckle noise is not a result of defects in an LDV, as no amount of manufacturing precision can eliminate speckle noise from LDV measurements. Essentially, speckle noise is itself another signal which must be removed.

Once I had discovered speckle noise, I had to answer two questions: how do I quantify speckle noise, and how do I eliminate it? Since I endeavored to quantify and remove speckle noise from an LDV recording seismic data kilometers away from an asteroid surface, I chose theoretical numerical simulations and computation experiments over lab based testing. Laboratory measurements would be taken at close range, and the measurements would include other vibrational noise sources in the room. Whereas adopting a computational experimentation framework allowed me to simulate a noiseless orbital environment to isolate the effect of laser speckle noise.

In my thesis, I endeavor to quantify and remove unwanted speckle noise from simulated orbital LDV data. To accomplish my goal, I combine three separate fields of study to make an incremental improvement to the design of an orbital seismometer. First, I studied the

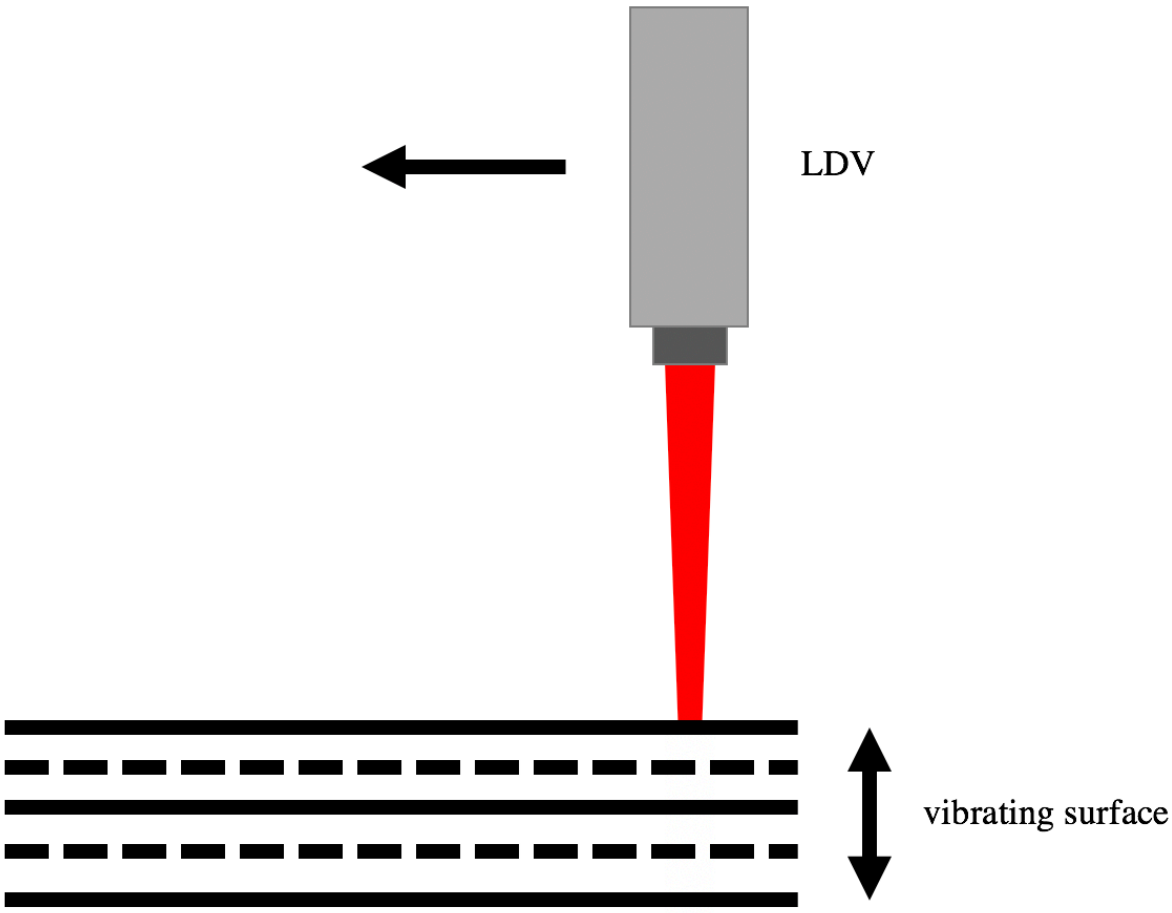


Figure 1.2: This thesis analyzes the noise that arises from transverse motion by an LDV over a rough surface, where the laser beam translates over the vibrating surface. The noise trace in Figure 1.3 is generated by acquiring data using this acquisition setup.

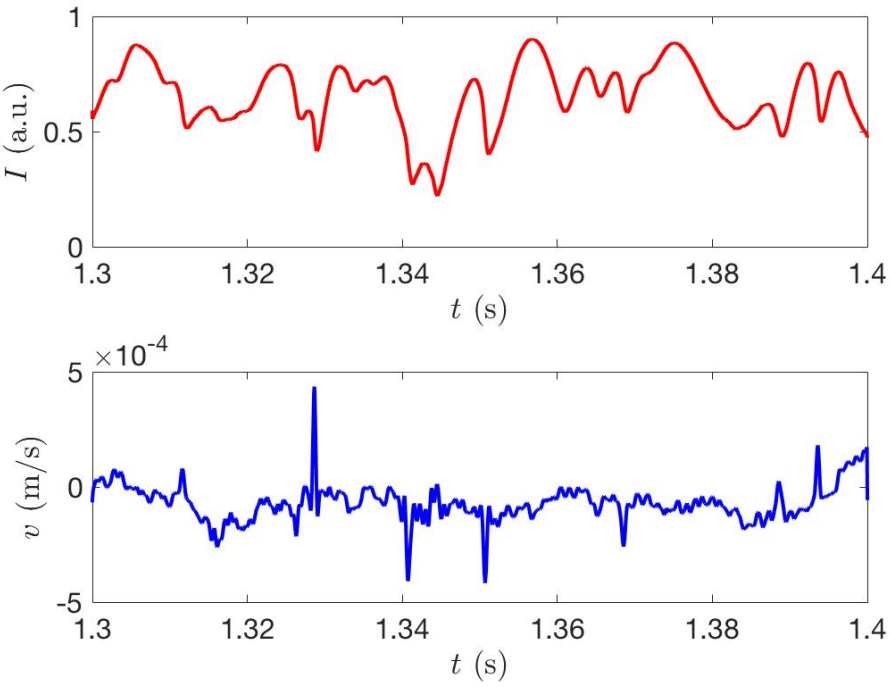


Figure 1.3: An LDV records two parameters as a function of time, (top) the intensity of reflected light off the target surface, and (bottom) the velocity component of the target in parallel with the LDV's laser beam. This figure shows a laboratory measurement of a motionless sample of asteroid regolith simulant while the LDV moves 10 cm/s translationally relative to the sample (no velocity in the direction of the beam). The LDV should record zero velocity, but instead records noise caused by the laser spot moving over the sample's rough surface. Significant noise is present in both the intensity and velocity signal.

fundamental physics behind laser Doppler vibrometry. How does one work? How does it record the velocity of the ground surface? How do rough surfaces affect LDV measurement accuracy? Such questions are addressed through the field of laser physics, and are addressed in Chapter 2.2. Once I understood the noise I was trying to remove, I studied the seismic signal that an orbital LDV would need to record. What would the seismic source be? How would the seismic source propagate through an asteroid? What would be the ground velocity signal that an orbital LDV would record? To answer these questions, I used principles from the field of seismology (Chapter 2.3). Having developed methods to simulate plausible noise and signal traces, I had one final question: how do I separate the laser speckle noise from the seismic noise? To accomplish this task, I built upon research in the signal separation field (Chapter 2.4).

The culmination of my research is a potential data acquisition scenario. A spacecraft releases an impactor upon the asteroid 101955 Bennu (Figure 1.4), generating a seismic source. The seismic waves propagate through the asteroid causing the far side to shake. Can an orbital LDV measure the seismic shaking despite laser speckle noise? My thesis provides an argument to answer, "yes".

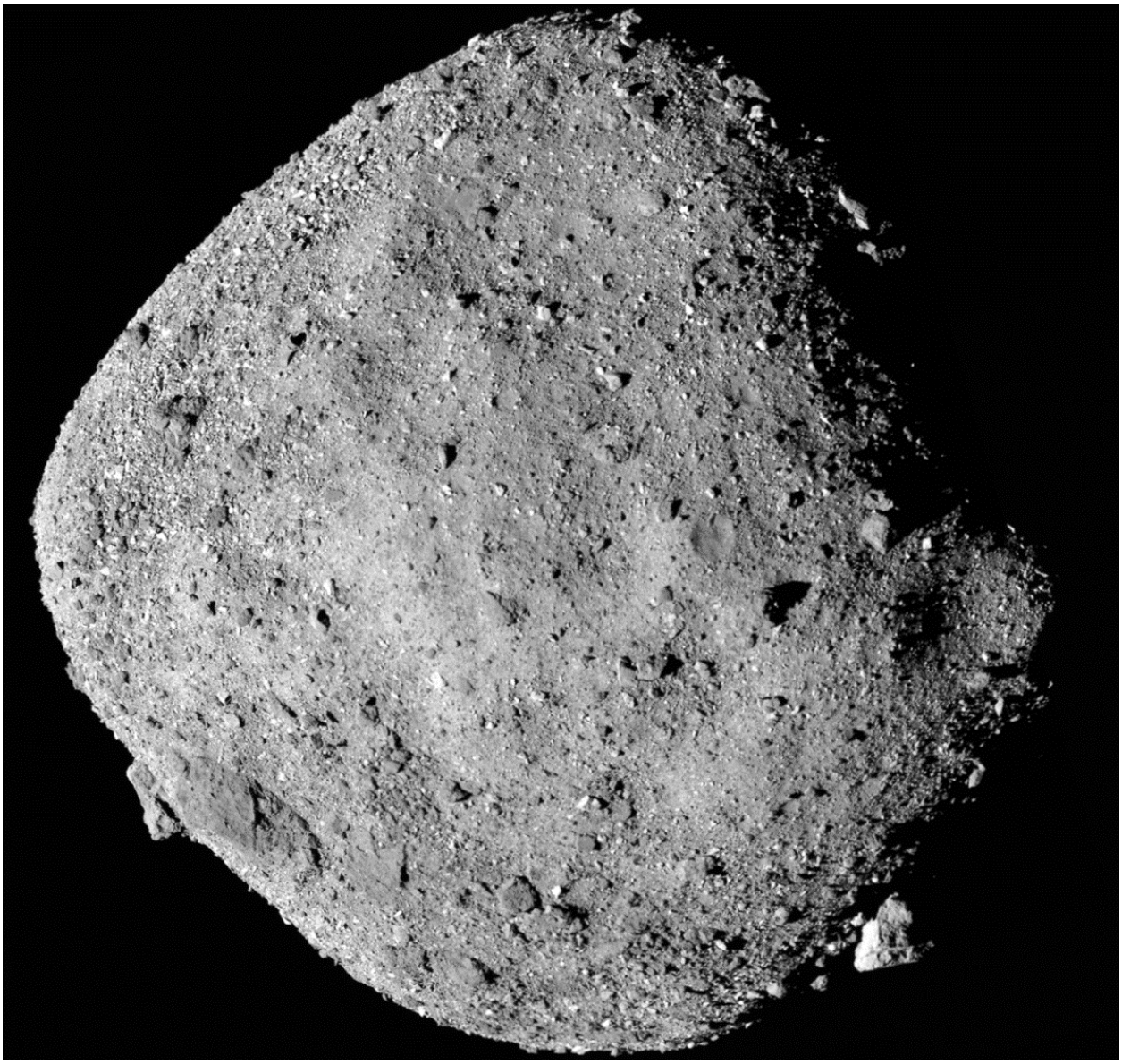

Figure 1.4: Asteroid 101955 Bennu: the hypothetical target of this thesis work. Credit: NASA/Goddard/University of Arizona.

# CHAPTER 2

# SPECKLE NOISE ATTENUATION IN ORBITAL LASER VIBROMETER SEISMOLOGY

To be submitted to *Advances in Space Research*

Samuel W. Courville[1][2] and Paul Sava[3]

The interior structures of small planetary bodies such as asteroids and comets are an enigma, yet understanding them has immense value. Knowing the internal structure is important for understanding the formation and evolution of the solar system and also has implications for in-situ resource exploitation and planetary defense from asteroids. Despite the immense value, no detailed investigation of the interior properties of an asteroid has yet been made. Although orbital radar and lander based seismological approaches have been proposed to make direct interior observations, it has not yet been demonstrated that radar could transmit through a rocky asteroid, nor that landing multiple seismometers is feasible or affordable. An elegant alternative to landed seismometers is orbital laser Doppler vibrometry, which could record seismic shaking of a small body without contact with the surface. Laser Doppler vibrometers (LDVs) are mature instruments for terrestrial applications; and could function similarly in a space environment. However, when incident on a rough surface like an asteroid regolith, an LDV is subject to laser speckle noise which may be misinterpreted as seismic shaking. We address the challenge of making LDV measurements on naturally rough surfaces by quantifying the laser speckle noise that an orbital LDV would encounter during a hypothetical orbital measurement. Specifically, we simulate an LDV measurement

[1]Graduate student, Center for Wave Phenomena, Colorado School of Mines, 1500 Illinois St., Golden, CO 80401, USA.
[2]Primary researcher and corresponding author
[3]Professor, Center for Wave Phenomena, Colorado School of Mines, 1500 Illinois St., Golden, CO 80401, USA.

of a seismic signal generated by an impact source on the asteroid 101955 Bennu. We demonstrate that speckle noise can be attenuated by combining multiple signals recorded by an orbital seismometer equipped with multiple LDV sensors. By mitigating laser speckle, we demonstrate that an orbital LDV can record seismic signals on a natural asteroid surface, which would enable an orbital seismometer to achieve the dense global coverage necessary for high resolution interior imaging.

## 2.1 Introduction

Small planetary bodies such as asteroids and comets are the building blocks of the solar system. Understanding how they form is key to understanding how the solar system formed and evolved (Asphaug, 2009; Scheeres et al., 2015). Small planetary bodies are akin to laboratories where we can test hypotheses of planetary accretion, from the particle scale upward. Questions about the origin of small bodies and planetary accretion often come down to understanding their internal structure (Asphaug, 2009; Scheeres et al., 2015). For example, there are several credible hypotheses for the interior structure of asteroids: rubble piles composed of gravitationally bounded impact shards, fractured monoliths that have remained largely intact despite impacts, or compactable fluffy regolith balls (Asphaug, 2009; Asphaug et al., 2002; Scheeres et al., 2015). Likely, the answer differs by asteroid type, and implies differing early solar system formation environments. In addition to scientific pursuits, knowledge of asteroid interior properties could also be useful for in-situ resource utilixation. Lastly, questions about the interior structure of asteroids are also important for planetary defense. Knowing their interior structure is required to deflect or disrupt asteroids on collision courses with Earth (Syal et al., 2016).

Our understanding of asteroid and comet interiors has significantly improved in recent years largely due to surface observations from recent missions (Scheeres et al., 2015). Over two dozen asteroids and comets have been visited by spacecraft to date, and another dozen are expected to be visited by spacecraft in the next decade (Barucci et al., 2011). Among the recent missions, NASA's Origins, Spectral Interpretation, Resource Identification, Se-

curity, Regolith Explorer (OSIRIS-REx) is exploring asteroid 101955 Bennu, which is now interpreted as a rubble pile through topographic analysis (Barnouin et al., 2019). Data from JAXA's Hayabusa2 spacecraft, including analysis from an impactor experiment that disrupted the near surface, suggests that asteroid 162173 Ryugu is also a rubble pile (Watanabe et al., 2019). ESA's Rosetta mission to the comet 67P/Churyumov–Gerasimenko revealed that the comet is likely a weakly layered agglomeration (Massironi et al., 2015). This interpretation is supported by bistatic radar data measurements, the only successful direct observations of a cometary interior to date (Ciarletti et al., 2017). Despite these impressive exploration advances, no detailed interior image of an asteroid's interior structure has been made to date (Herique et al., 2018; Sava and Asphaug, 2019). Advances in numerical modeling allow for the development of internal structure hypotheses that can explain surface observations, but these hypotheses can not be tested without direct measurements. The interior structure of small bodies remains terra incognita (Asphaug, 2009).

Planetary science goals would greatly benefit from methodology to image the interiors of small planetary bodies. Recognizing the scientific value of making direct measurements of small body interior properties, various authors have proposed missions with sounding instruments to peer inside small bodies (Scheeres et al., 2015). Building off of the bistatic radar experiments conducted by ESA's Rosetta mission, Asphaug et al. (2014), Sava et al. (2015), Sava and Asphaug (2018a), and Sava and Asphaug (2018b) have proposed radar imaging. Although radar waves can propagate several kilometers through icy material, they rapidly attenuate in solid rock (Grimm et al., 2015). This means that although radar may be a valid solution for imaging icy comets, it remains to be demonstrated that it is a viable option for imaging rocky asteroid interiors.

Seismology provides an attractive alternative to radar. Whereas radar is sensitive to electromagnetic properties, which may not be correlated to geologic structure, seismic waves are sensitive to properties such as density and compressibility, which are directly related to the interior structure and strength (Sava and Asphaug, 2019). Richardson et al. (2005) and

Asphaug (2008) have demonstrated that seismic waves propagating through asteroids, e.g. generated by impacts, can cause global surface disruption. Using empirical and numerical models, the observed surface disruption can be related to the bulk interior properties (Asphaug, 2008). However, this method is still an indirect interpretation of the interior. A more robust option is to directly observe seismic propagation through asteroids, for example using landed seismometers on an asteroid (Plescia et al., 2018). Landed seismometers could record seismic waves that have propagated through the center of an asteroid. However, this approach is technically challenging because multiple seismometers must land across the surface of the asteroid (Plescia et al., 2018). Additionally, it is unknown whether a seismometer resting on the surface of an asteroid would be coupled well enough to make useful seismic measurements (Sava and Asphaug, 2019).

Orbital seismology is a more elegant solution with significant advantages over lander based seismology. Instead of landing seismometers, Sava and Asphaug (2019) propose to use laser Doppler vibrometers (LDVs) for non-contact remote sensing of seismic signals. By shining a laser on a vibrating object and recording the Doppler shift of the light that reflects back, an LDV can measure the velocity of the object. LDVs are a well developed instrument and enjoy a wealth of applications on earth including structural health monitoring and manufacturing component testing (Castellini et al., 1998; Rothberg et al., 2017; Staszewski et al., 2012). Equipped with LDVs, a spacecraft can achieve global seismological coverage of a small body without ever landing on the surface. Sava and Asphaug (2019) show that LDV measurements of seismic signals at multiple locations over an asteroid's surface can make a 3D image of its interior properties.

Sava and Asphaug (2019) propose that an orbital LDV could make non-contact seismic measurements of an asteroid, but leave to future analysis to determine how LDVs would function on natural asteroid surfaces, which is a key aspect of orbital seismology. Without the ability to operate on rough surfaces, LDVs could not achieve dense measurement coverage over a small body because coverage would be limited to wherever laser retroreflectors could

be deployed across its surface. To reap the full benefits of an orbital seismometer, the instrument must be functional on natural surfaces. Whereas LDV's can achieve nm/s or better resolution in low noise settings, they are subject to so-called speckle noise when in motion relative to a rough target surface (Rothberg et al., 2004). This noise is a result of constructive and destructive interference of light reflected by surfaces with roughness greater than the wavelength of the laser (Drabenstedt, 2007). In this paper, we quantify laser speckle noise and design methods to separate it from seismic signals in order to bolster the orbital seismology concept proposed by Sava and Asphaug (2019).

Through numerical simulations, we demonstrate that accurate seismic measurements in the presence of speckle noise are possible from an orbital LDV acting on natural asteroid surfaces. We first discuss the methodology needed to predict the speckle noise produced by orbital motion of an LDV over a rough natural surface. Next, we analyze characteristics of possible seismic signals that an LDV would need to record. There are several potential natural and artificial seismic sources to consider on a small body. Natural sources might include tidal forces inducing natural microseismic events, outgassing from a comet generating slight shaking, or the jolt from an impact (Binzel et al., 2010; Richardson et al., 2005). Artificial sources could be based on chemical explosives as occasionally used in seismic exploration on Earth (Aki and Richards, 2002), or artificial impacts (Saiki et al., 2013). In our study, we focus on artificial sources given our greater ability to predict and control their location and magnitude. We specifically assume an impact source similar to the Small Carry-on Impactor (SCI) experiment on JAXA's Hayabusa2 mission, which demonstrated the plausibility artificial seismic sources with small spacecraft add-ons (Saiki et al., 2013). Finally, using the signal and noise estimates, we show that speckle noise can be separated from the seismic signal through signal diversity combining. Thus, this paper is organized into three major sections addressing the questions:

1. What is the speckle noise inherent in an orbital measurement? (Section 2.2)

2. What is the seismic signal we expect to record from an impact source? (Section 2.3)

3. How do we separate the seismic signal from the speckle noise? (Section 2.4)

We demonstrate the separation of speckle noise from seismic signals, using a seismic data acquisition scenario over the asteroid 101955 Bennu (Figure 2.1). We consider an LDV orbiting the asteroid at a distance of 2 km above the surface. Given the mass of 101955 Bennu, this yields an orbital velocity of approximately 5 cm/s, which is similar to the orbital velocity of OSIRIS-REx (Daly et al., 2017). We assume that the laser spot point moves across the surface at the same speed as the spacecraft orbits. In reality, the spot might move slower or faster depending on the rotational velocity of the asteroid in relation to the chosen orbit. Lastly, we assume that a seismic impact source is located on the opposite side of the asteroid and is generated from an impactor similar to Hayabusa2's SCI.

## 2.2 LDV speckle noise simulation

### 2.2.1 LDV theory

In this section, we briefly review laser Doppler vibrometer (LDV) theory. An LDV measures the velocity of a target object by shining a laser on the object and recording the Doppler shift of the reflected laser light caused by the target's motion. LDVs are mature instruments, and a full description of how they function can be found in Donges and Noll (2015). An LDV uses a laser of known wavelength that is split into two beams. One beam remains in the LDV as a reference, and the other is directed to the target surface where it is reflected (Figure 2.2). If the target is moving in-line with the beam, the reflected light is Doppler shifted relative to the incident beam by

$$\Delta f = f_r - f_i = \frac{2v}{\lambda_i}, \tag{2.1}$$

where $f_r$ and $f_i$ are the frequencies of the reflected and incident beams, respectively, $v$ is the surface velocity component parallel with the incident beam, and $\lambda_i$ is the wavelength of the incident laser beam (Donges and Noll, 2015; Sava and Asphaug, 2019). As shown in Figure 2.2, the LDV measures the frequency of the reflected beam by recording the light intensity of the interference between the reference and reflected beam, a method known as

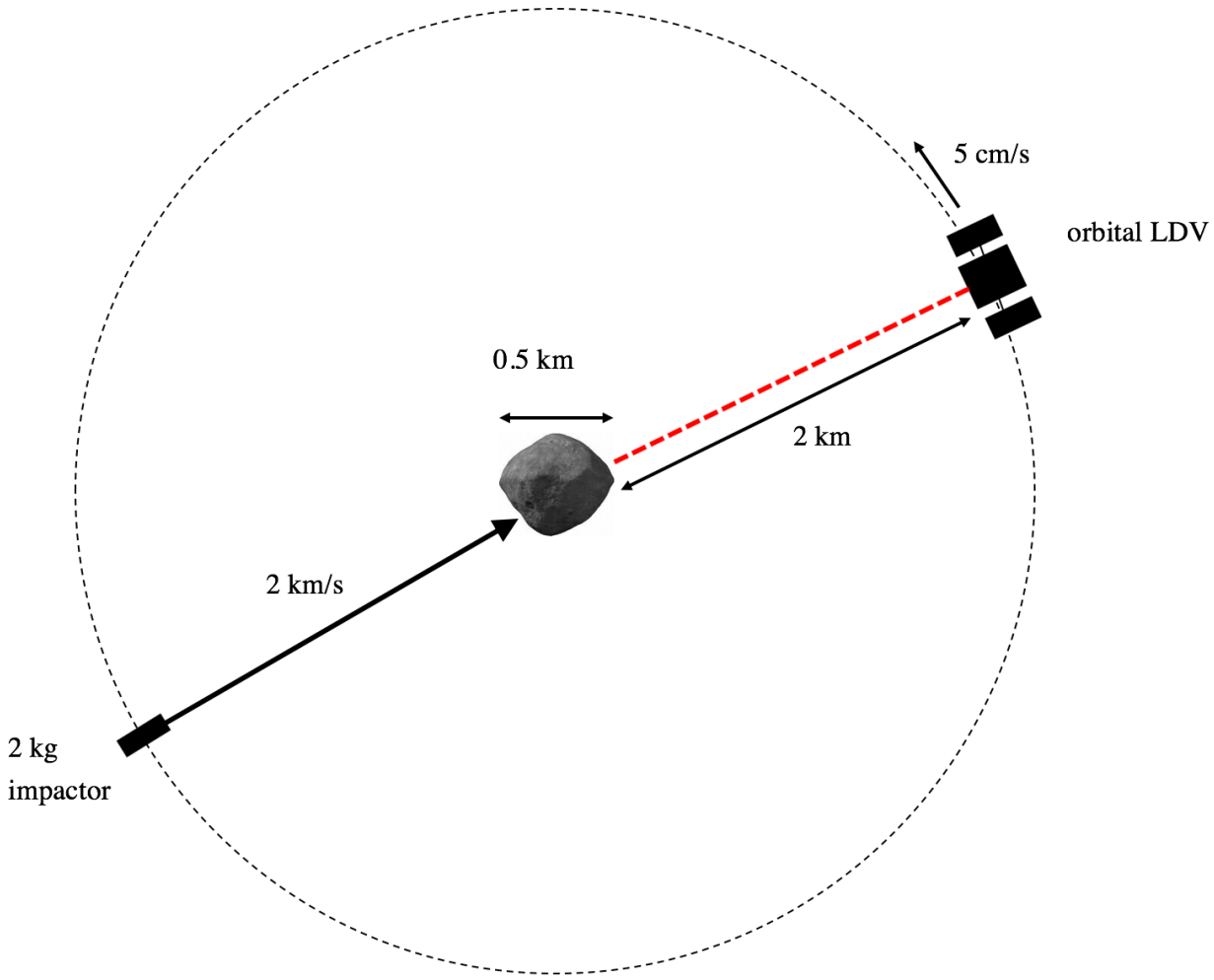


Figure 2.1: The seismic data acquisition scenario. We simulate an LDV orbiting with a velocity of 2.5 cm/s at a distance of 2 km from the surface of 0.5 km wide asteroid 101955 Bennu. The impactor weighs 2 kg and travels at 2 km/s upon impact with the surface.

optical heterodyning. As derived in Donges and Noll (2015) and Sava and Asphaug (2019), the light intensity recorded at the LDV's detector is a function of the surface velocity,

$$I(t) = I_r + I_i + 2\sqrt{I_r I_i}\cos\left[2\pi \int \left(\frac{2v(t)}{\lambda_i} + f_0\right)dt + (\phi_i - \phi_r)\right], \tag{2.2}$$

where $\phi_i$ and $\phi_r$ are the starting phases of the incident and reflected beams respectively, and $f_0$ is a known frequency shift applied to the reference beam through a Bragg cell (Donges and Noll, 2015). The integral accounts for the accumulated phase shift in the reflected light as the surface moves with velocity $v$. As a whole, Equation 2.2 describes a frequency modulated signal with a carrier frequency $f_0$ and a modulation given by Equation 2.1. To recover the velocity of the surface, one must demodulate the intensity signal with the known carrier frequency, $f_0$.

### 2.2.2 Laser speckle patterns

Equation 2.2 assumes that the target behaves like a mirror, where the light is reflected specularly and remains spatially coherent over the size of the LDV's detector. Light is said to be spatially coherent if each location in the light's wavefront has the same phase (Thompson et al., 2017). Any spatial incoherence in the reflected wavefront can reduce the power and accuracy of the resulting LDV velocity measurement. To behave like a mirror, an object must have surface roughness that is less than the wavelength of the incident light (Drabenstedt, 2007). In this paper, we quantify the surface roughness as the root mean square (RMS) deviation from the average surface height. We classify a rough surface as one with roughness greater than 775 nm, which is the wavelength of the laser considered in this study. After reflection from such a rough surface, laser light becomes spatially incoherent because the rough surface acts as an incoherent source (Drabenstedt, 2007). The Van Cittert-Zernike Theorem states that light from an incoherent source, such as the reflectance from a rough surface, only appears spatially coherent if the following condition is satisfied,

$$r \gg \frac{d^2}{\lambda}, \tag{2.3}$$

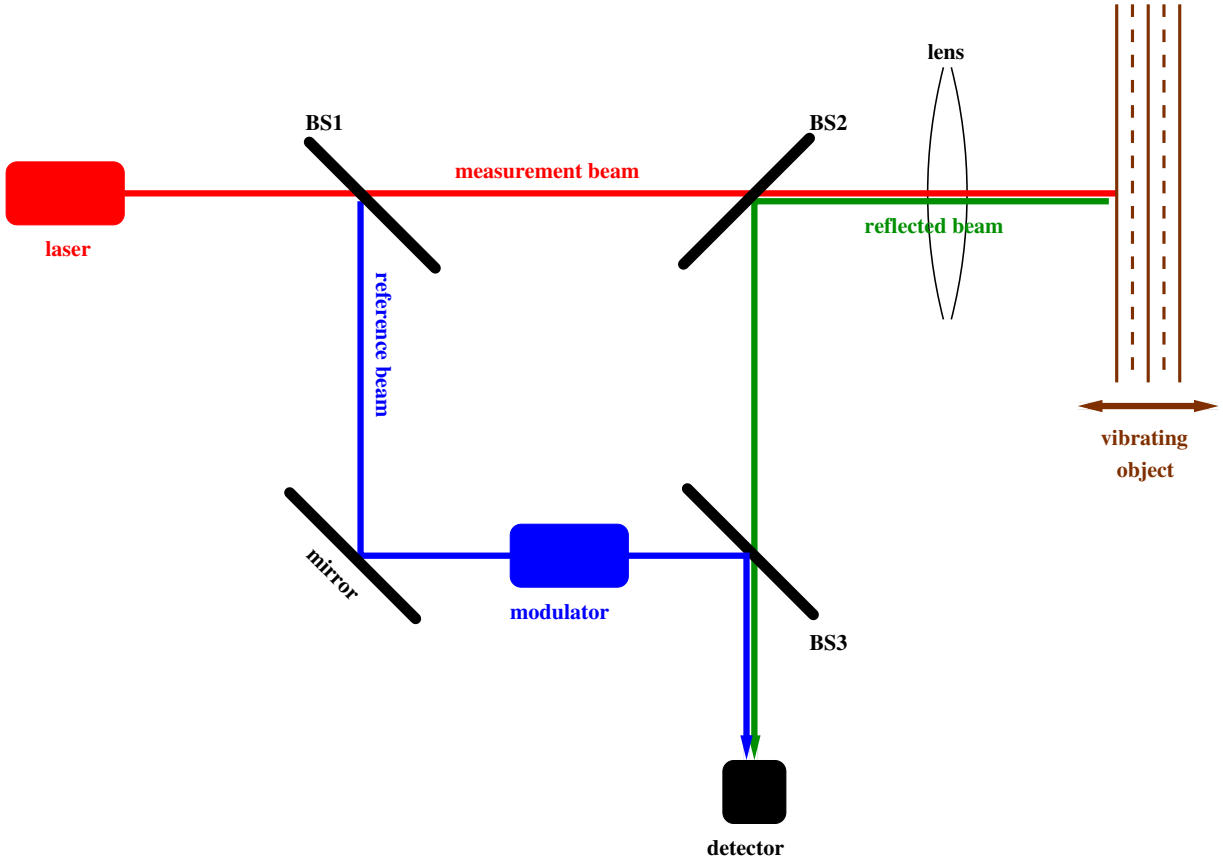


Figure 2.2: A schematic of a Laser Doppler Vibrometer (LDV). The original laser beam is split into a measurement and reference beam at the first beam splitter (BS1). The measurement beam is directed at a vibrating target. In-line motion of the target Doppler shifts the frequency of the reflected beam. Upon return, the reflected beam is redirected by BS2 toward the detector. BS3 combines the reflected and reference beams. Due to the frequency shift of the reflected beam, the combined beams produce time dependent interference (optical heterodyning), which contains information about the surface motion (Equation 2.2)

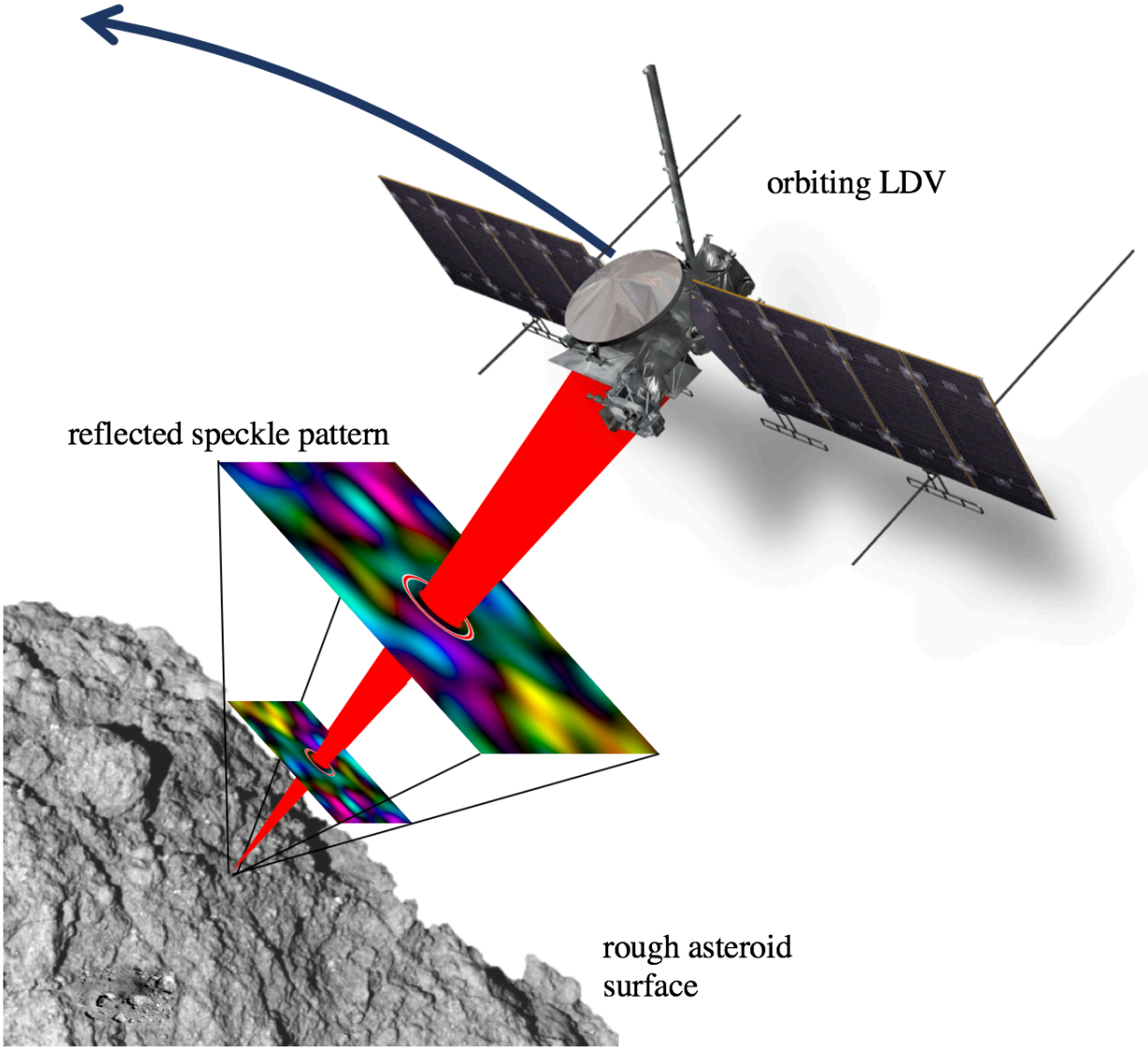


Figure 2.3: Illustration of how a coherent laser beam is reflected as an incoherent speckle pattern if the surface is rough. Not to scale; the beam and speckle sizes are exaggerated.

where $r$ is the distance to the surface, $d$ is the diameter of the detector, and $\lambda$ is the wavelength of the laser light (Thompson et al., 2017). This condition is not satisfied under our acquisition scenario where $r = 2$ km, $\lambda = 775$ nm, and $d$ is similar to typical LDV aperture sizes of a few centimeters (Dräbenstedt et al., 2012). Thus, if the asteroid's surface is rough, the reflected light returning to the detector is no longer spatially coherent. The spatial incoherence manifests as a laser speckle pattern (Rothberg et al., 2004), pictured in Figure 2.3. The LDV detector samples a portion of the reflected speckle pattern.

To simulate a speckle pattern, we approximate a rough surface as a collection of Lambertian tiles. Constructive and destructive interference at the detector from ray paths originating at tiles with different path lengths, as a result of surface roughness, produces a speckle pattern. The reflected electric field from the $j^{th}$ tile observed at a location $(x, y)$ on a detector plane located a distance $z$ above the target surface is

$$\mathbf{E}_j(x, y) = C_j(x, y)\hat{\mathbf{E}}_0 e^{i(kr_j(x,y)+2\pi ft+\phi_i)}, \tag{2.4}$$

where $\hat{\mathbf{E}}_\mathbf{0}$ denotes the unit vector polarization of the starting laser beam (we assume linear polarization), $k$ denotes the laser wavenumber, $r_j(x, y)$ is the distance between the $j^{th}$ surface tile and the $(x, y)$ location on the detector plane, $f$ is the frequency of light, $\phi_i$ is the initial phase of the incident beam, and $C_j$ is a scaling factor (Figure 2.4). This model does not consider multiple scattering, and thus the reflected light retains the same polarization as the incident beam. In reality, reflected laser light from a scattering surface may become depolarized Morgan and Ridgway (2000). For our purpose, this can be effectively approximated by assigning a random polarization vector to each tile. Since light is a transverse wave and the LDV is positioned kilometers away from a centimeter scale laser spot, the z component of the polarization is many orders of magnitude less than the polarization in x or y, and can be ignored. The scaling factor

$$C_j(x, y) = \left(\frac{\alpha_j}{2\pi(r_j(x, y))^2}\right)\left(\frac{2P_0}{\pi w^2}\right)e^{-2\frac{d_j^2}{w^2}}, \tag{2.5}$$

accounts for the percent amplitude of light reflected by the $j^{th}$ tile with albedo ($\alpha_j$), the spherical geometrical spreading, and the power of the incident beam's Gaussian profile. The variable $w$ is the $1/e^2$ beam diameter[1], $d_j$ is the $j^{th}$ tile's distance from the center of the beam profile, and $P_0$ is the incident beam peak power. Since we are only interested in the relative phases from each tile, we can ignore the time dependency and assume $\phi_i = 0$, thus simplifying Equation 2.4 to,

$$\mathbf{E}_j(x,y) = C_j(x,y)\hat{\mathbf{E}}_0 e^{ikr_j(x,y)}. \tag{2.6}$$

The total electric field at each detector point $(x, y)$ is given by the sum of the electric fields from all $n$ surface tiles,

$$\mathbf{E}(x,y) = \sum_{j=1}^{n} \mathbf{E}_j(x,y). \tag{2.7}$$

The intensity of light at each detector location is given by,

$$I(x,y) = \frac{c\epsilon_0}{2}|\mathbf{E}(x,y)|^2, \tag{2.8}$$

and the phase by,

$$\phi(x,y) = \tan^{-1}\left(\frac{\mathrm{Im}(\mathbf{E}(x,y))}{\mathrm{Re}(\mathbf{E}(x,y))}\right), \tag{2.9}$$

where $c$ is the speed of light and $\epsilon_0$ is the vacuum permittivity.

Using Equations 2.8 and 2.9, we simulate speckle patterns from surfaces in different surface roughness regimes. Figure 2.5 illustrates that speckle patterns only develop when the surface roughness is greater than the light's wavelength. As mentioned previously, If the surface has roughness less than the wavelength of light, the surface acts like a mirror. We also generate speckle patterns from surfaces with similar surface roughness (RMS height variation), but with different lateral roughness(distance between topographic high points). Figure 2.6 shows that the size and intensity of the speckles remain similar for surfaces with different lateral heterogeneity. This observation agrees with Drabenstedt (2007) and Guo

[1]The $1/e^2$ radius of a laser beam with a Gaussian profile is the distance from the center of the laser beam to the point at which the intensity of the beam falls to $1/e^2$ ($\approx$0.135) of the peak intensity of the beam.

et al. (2001), who show that, counter-intuitively, speckle pattern statistical properties are independent of the surface roughness properties, provided the roughness is greater than the light wavelength. In general, the mean speckle diameter, $d_s$, is given by,

$$d_s = \frac{2\lambda_i r}{\pi w} \tag{2.10}$$

where $\lambda_i$ is the laser wavelength, $r$ is the distance to the target surface, and $w$ is the $1/e^2$ diameter of the laser beam on the target surface (Drabenstedt, 2007). For our study, we consider an LDV with a $1/e^2$ laser beam radius of 2.5 cm on the surface, which is consistent with existing long range LDVs (Dräbenstedt et al., 2012). In order to isolate the effect of laser speckle, we assume that there is no noise from background light, electrical components in the LDV, optical imperfections in the instrument, fluctuations in the LDV output laser beam, or instability of the spacecraft (jitter).

Do we expect rough surfaces on asteroids and comet surfaces? All current observations of small bodies say, "yes." From the first Hayabusa mission, it is known that 25143 Itokawa is largely composed of grains greater than 1 mm in size, with the spacecraft returning some grains with diameters on the order of 10s of microns back to Earth (Yoshikawa et al., 2015). Observations from Hayabusa 2 show a similar story for 162173 Ryugu, where the smallest grain size appears to be on the order of 1-10 mm (Hamm et al., 2018). The recent arrival of OSIRIS-REx at asteroid 101955 Bennu has revealed that its surface is even coarser, dominated by pebbles with cm scale roughness (Lauretta et al., 2019). Thermal inertia and polarimetry studies of larger asteroids, like 4 Vesta, show that smaller grains on the order of 10s of microns could be present (Benner et al., 2015; Delbo et al., 2015). Although it might be postulated that specular reflections could be present on comets with high ice content, the dust analyzer on the Rosetta spacecraft measured grains with sizes from 100s of $\mu$m to mm in size, and demonstrated that the comet was more dusty than icy. Thus, we can assume that all known asteroid and comet surfaces exhibit surface roughness that is greater than the LDV wavelength. An exception may be the metallic surface of an asteroid like 16 Psyche (Matter et al., 2013), though this is highly speculative.

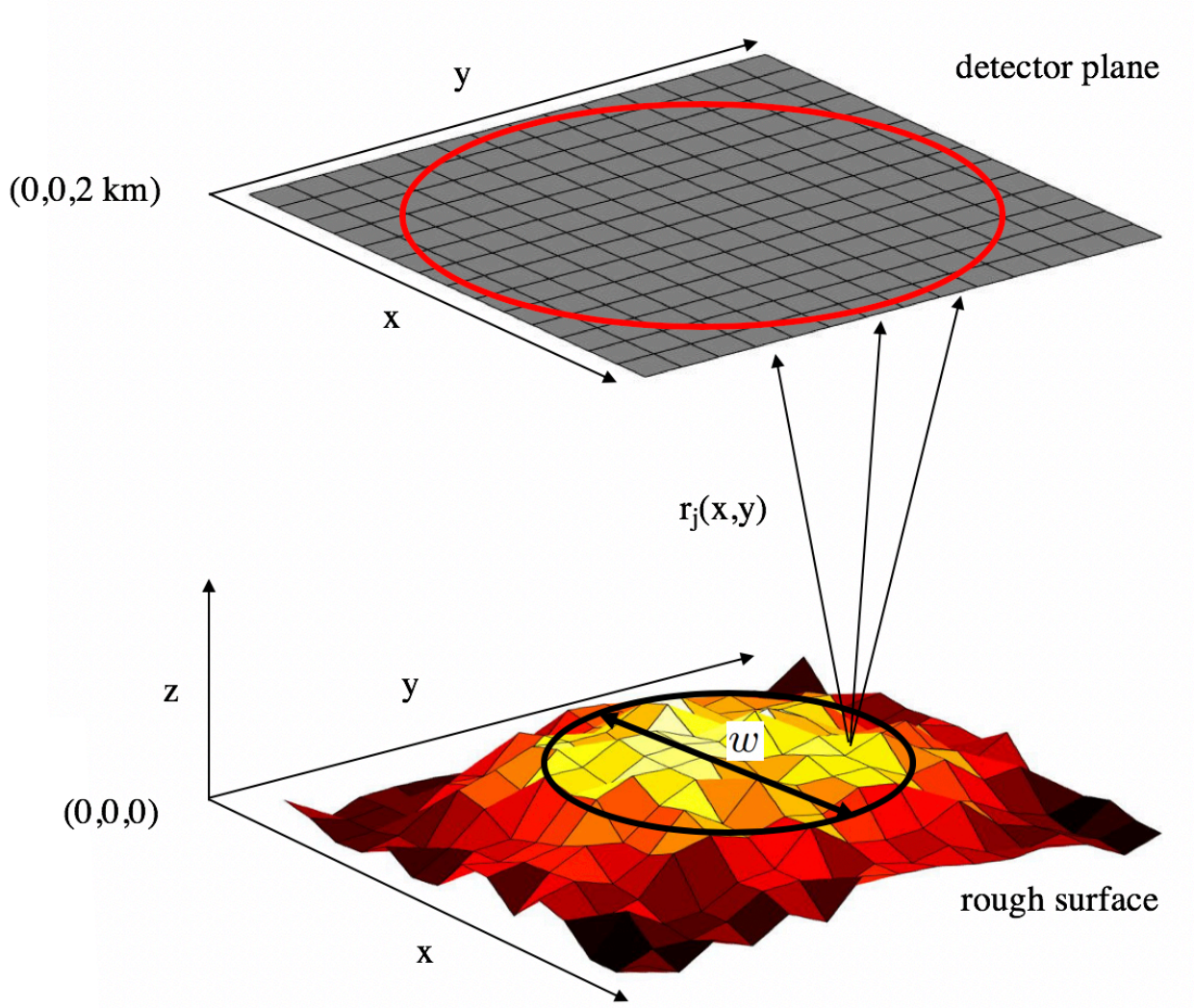


Figure 2.4: Illustration of speckle pattern computation from a rough surface (not to scale). Each surface tile contributes to the electric field recorded at the detector plane. The detector plane is 2 km above the rough surface. The red circle indicates the area of the LDV detector. The black circle with diameter $w$ indicates the $1/e^2$ Gaussian beam footprint.

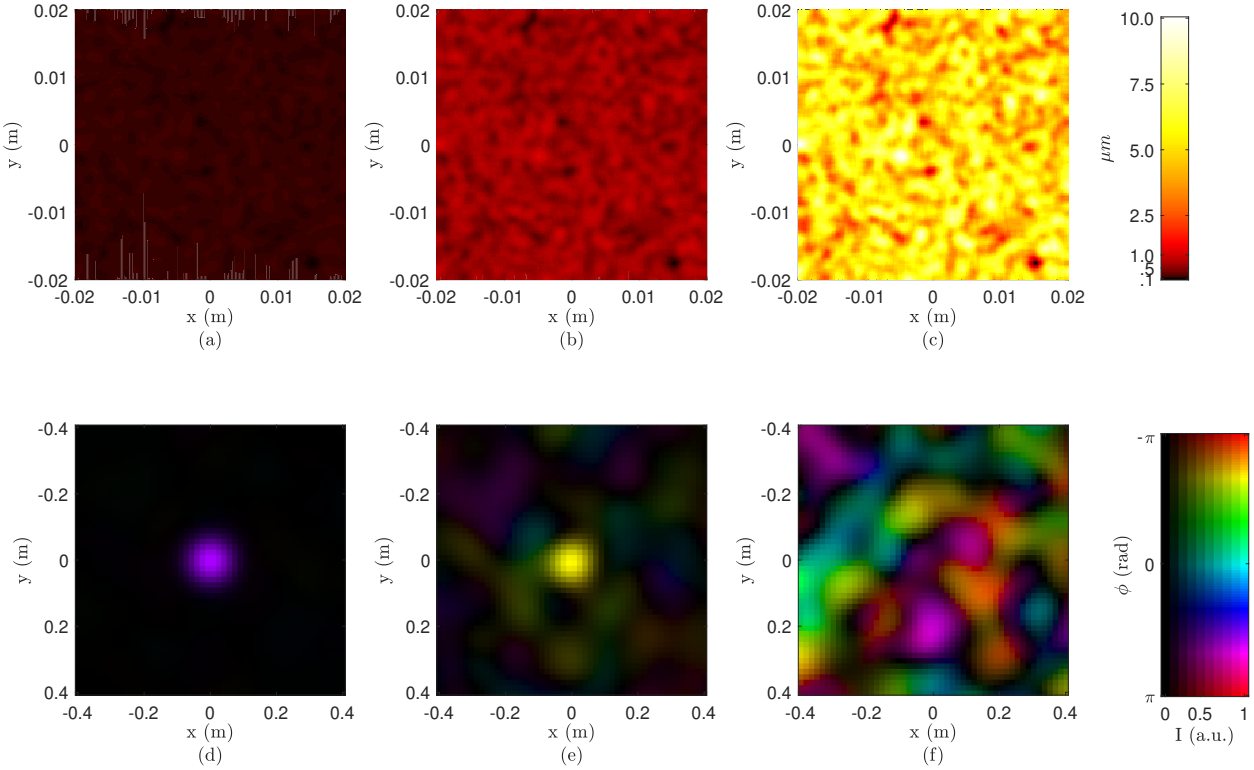


Figure 2.5: Panels (a), (b), and (c) show random rough surfaces with peak relief of $10^{-7}$, $10^{-6}$, and $10^{-5}$ meters, respectively. Panels (d), (e), and (f), display the reflected light recorded at a detector 2 km away for the corresponding surfaces (a), (b), and (c). The simulated laser has a Gaussian beam profile with a $1/e^2$ radius of 2.5 cm, and a wavelength of 775 nm. When the surface roughness is less than wavelength (a), the surface acts as a mirror, and the beam profile is simply reflected (d). When the surface roughness is on the same order of magnitude as the laser wavelength (b), the reflected light has a bright center and a faint interference speckle pattern around it (e). For roughness much greater than the wavelength (c), a full speckle interference pattern develops (f).

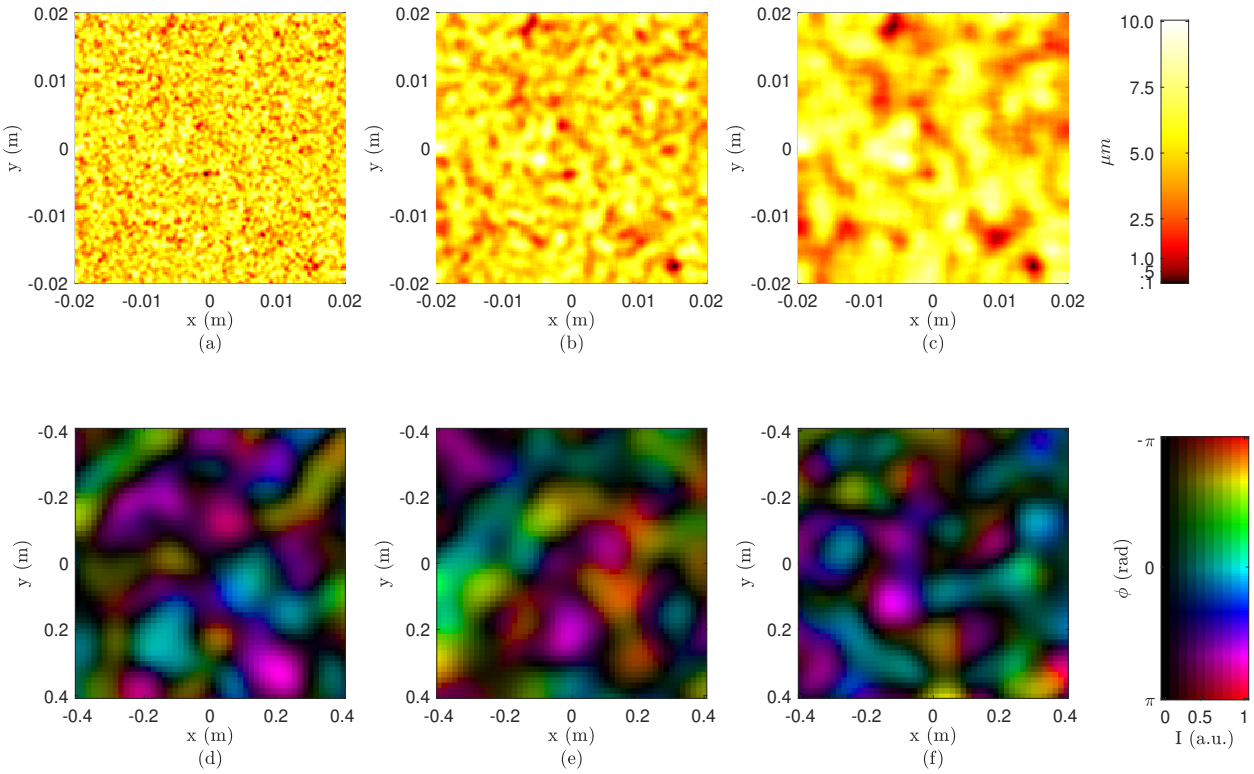


Figure 2.6: Illustration of the property that speckle patterns are independent of the lateral roughness scale. The speckle pattern (d) from a rough surface with grains that are approximately 0.5 mm across (a) is statistically indistinct from speckle patterns (e) and (f), which were produced by grains that are 1 mm (b) or 5 mm across (c).

### 2.2.3 Speckle induced measurement error

When a stationary LDV points at a rough surface, speckle patterns are not a significant concern. If the detector happens to record a dark speckle location, the operator can simply re-aim the LDV until a bright speckle is sampled. However, if the observed speckle pattern changes with time, it is challenging to ensure a bright speckle would be sampled at all times. An evolving speckle pattern causes velocity measurement errors and signal dropouts as bright and dark speckles of the reflected light move over the detector.

Intuitively, the magnitude and frequency of the speckle noise depends on the speed at which an LDV moves relative to the surface. The faster the LDV spot moves across the surface, the faster the speckle pattern changes. We can quantify the noise affecting an orbital LDV based on the expected orbital velocity of a spacecraft relative to an asteroid. Figure 2.7(b) illustrates a simulated velocity measurement as an LDV moves laterally at 5 cm/s over a motionless surface shown in Figure 2.7(a). Note that the LDV records vertical velocity even though it should record no motion since the surface is static. The noise is uncorrelated with the surface profile. The only location where the noise subsides is at the location where the surface roughness drops below the wavelength of the laser light. This agrees with the literature that demonstrates speckle patterns to be independent from local surface properties, provided roughness is present (Drabenstedt, 2007; Guo et al., 2001).

To better understand how speckle noise occurs, Figure 2.8 illustrates three time steps of an evolving speckle pattern as a laser beam moves at 5 cm/s across a stationary surface. As the speckle pattern changes, the intensity and the phase recorded by the detector changes. Figure 2.9 tracks the change in intensity and phase as a function of time as the laser spot moves across the rough surface. The phase changes most rapidly when the intensity is low. When the intensity is near zero, it only takes the contribution of one new surface tile to change the phase. When the intensity is high, many surface tiles are already in phase with each other, and one new surface tile cannot disrupt this coherence. Since the surface is stationary in this simulation, the LDV should record a constant zero velocity. However,

because changing phase from an evolving speckle pattern appears the same as a frequency change, the LDV interprets it as a Doppler shift, and records an erroneous surface velocity. The velocity error is largest when the phase changes most rapidly, and the phase changes most rapidly when the intensity is low. The noise is characterized by smooth oscillations with occasional large spikes. The magnitude and frequency of the speckle noise becomes larger the faster the orbital velocity. By visual inspection of Figure 2.9, it is apparent that intensity is a proxy for the variance of the speckle noise, as also demonstrated theoretically by Dräbenstedt (2014).

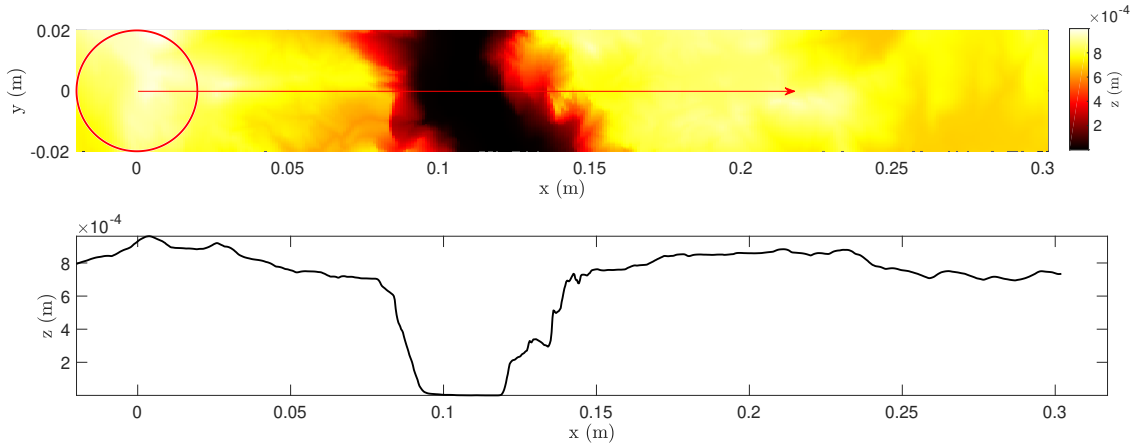


(a)

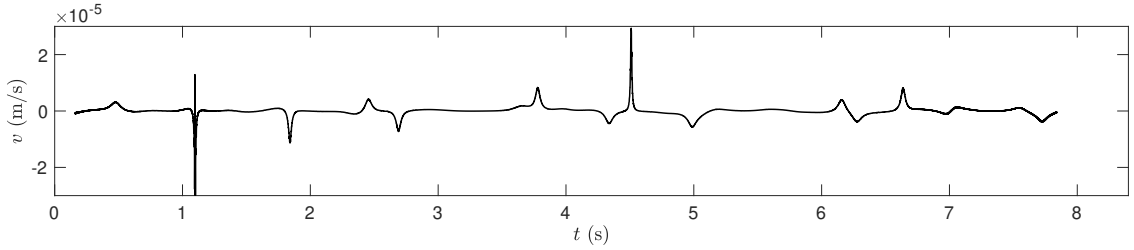


(b)

Figure 2.7: (a) An example of rough topography (map and profile view) with multiple different scales of roughness. We simulate an LDV velocity measurement from a distance of 2 km as the laser spot moves across the map from left to right at a velocity of 5 cm/sec. The red circle on the map view indicates the $1/e^2$ radius of the Gaussian laser spot. The surface is motionless. (b) Erroneous LDV velocity measurement from surface roughness induced speckle noise.

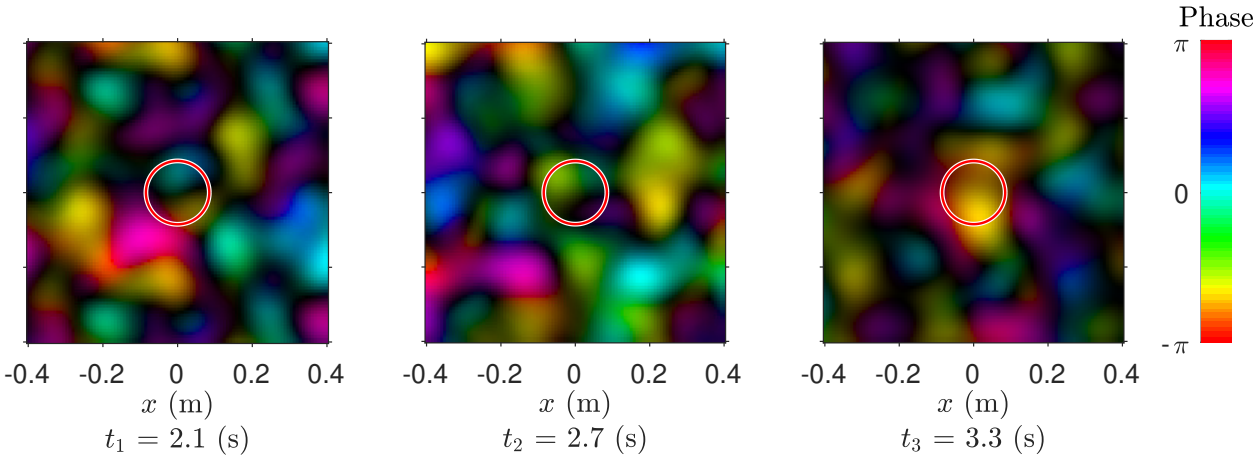


Figure 2.8: Speckle patterns for the case when the laser spot moves across a rough surface at 5 cm /sec. The red circle indicates the detector size. $t_1$, $t_2$, and $t_3$ correspond to times when the detector records a dark, medium, and bright portion of the speckle pattern.

Using the acquisition scenario outlined in Figure 2.1, Figure 2.10 shows three realizations of plausible speckle noise. This noise is inherent in the physics of an LDV operating on a rough surface. The large noise spikes occur randomly, and it is unlikely for large spikes to occur at the same time between multiple concurrent measurements.

### 2.2.4 Speckle noise reduction

We propose two ways to reduce speckle noise: (1) accurate spacecraft control, and (2) signal processing algorithms. For the first strategy, we suggest that the orbital LDV should be operated to minimize the motion of the laser spot on the surface. Designing the LDV so it can target a fixed point during a measurement could reduce speckle noise, albeit not eliminate it completely. An evolving speckle pattern would still occur because the detector plane moves relative to individual scattering points on the surface as the spacecraft rotates to aim the laser spot at the same ground location. Figure 2.11 illustrates that the RMS speckle noise scales linearly with orbital velocity in either the translational or rotational cases; however, the slope for rotational case is significantly smaller. For the remainder of our paper, we assume a worst case scenario, in which the spacecraft makes no attempt to point at the same surface location.

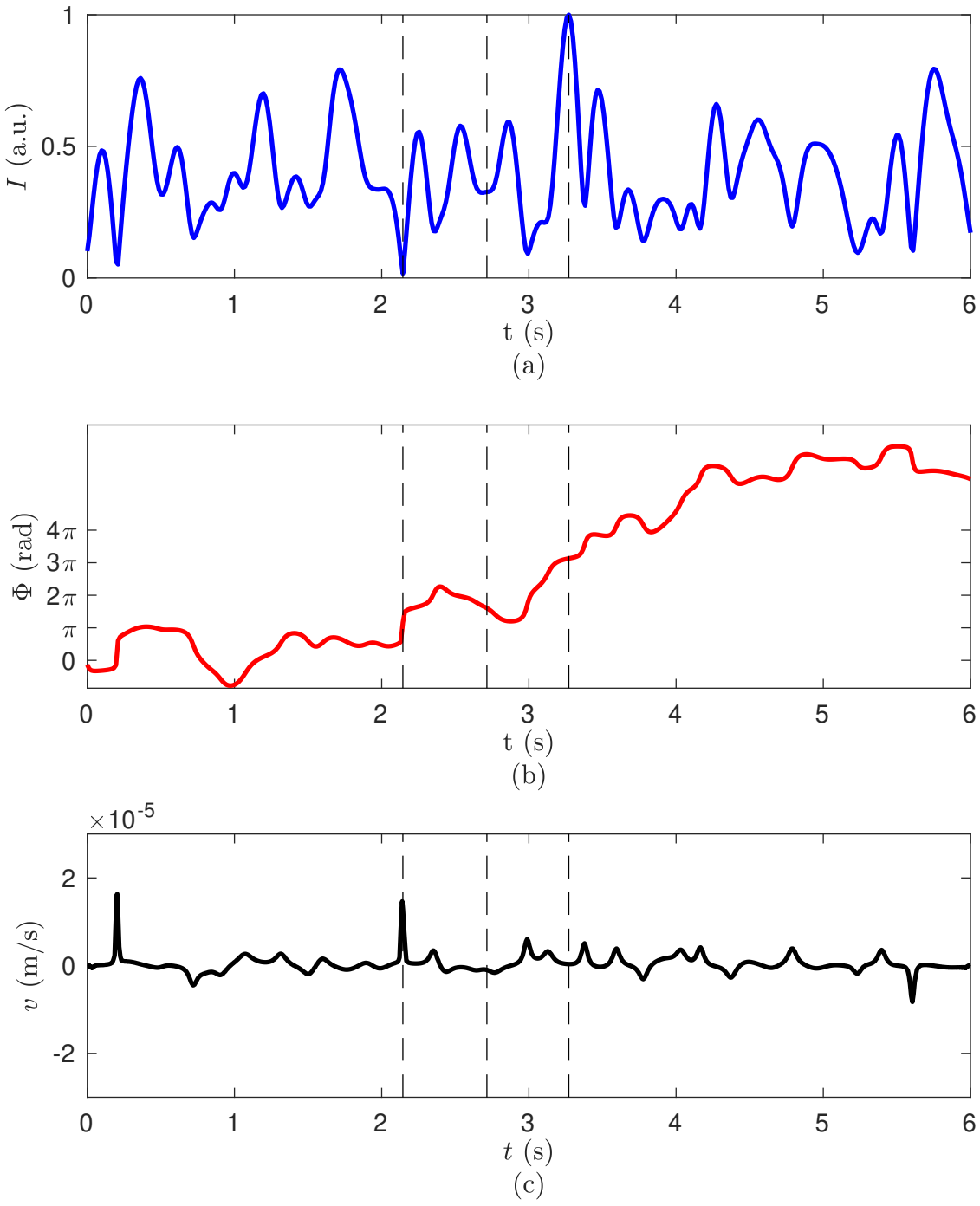


Figure 2.9: (a) Illustration of LDV intensity recorded as a function of time, (b) the relative phase as a function of time, (c) and the erroneous velocity recorded by the LDV due to the variable phase. The dashed lines correspond to $t_1$, $t_2$, and $t_3$ in the speckle images in Figure 2.8. The velocity signal has peaks when the phase changes quickly; the phase changes the quickest when the signal intensity is low.

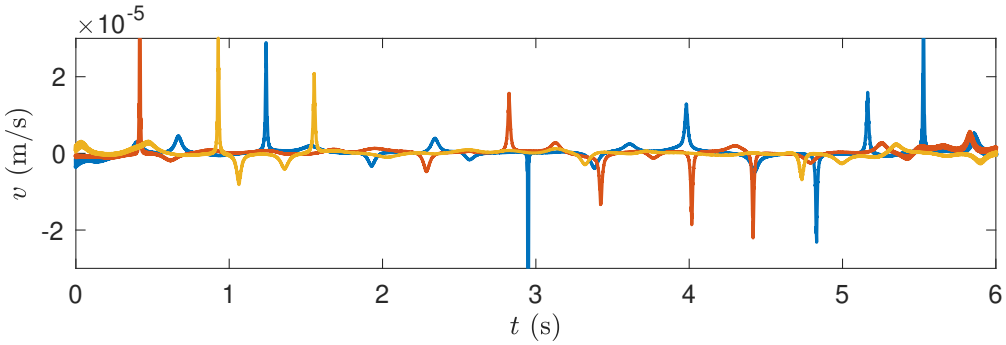


Figure 2.10: Each different color curve corresponds to a realization of LDV speckle noise from an orbital LDV placed at 2 km from the surface and orbiting at 5 cm/s as depicted in Figure 2.1.

Alternative to physically reducing speckle noise through spacecraft operation, we consider signal processing algorithms. The seismic signal and the speckle noise can be separated by taking advantage of the different properties of the signal and noise. The remainder of this paper outlines how to describe impact-induced seismic signals and how to separate seismic signals from speckle noise based on their attributes.

## 2.3 Impact seismic signal simulation

### 2.3.1 Impact source

To properly consider how to separate speckle noise from seismic signals, we need a model of the ground motion signal as a function of time. We consider an impact source for two reasons: 1) natural impacts have occurred on asteroids, and several studies suggest that they can induce global surface shaking at the asteroid surface (Quillen et al., 2019; Richardson et al., 2005); and 2) synthetic impacts on an asteroid surfaces have been demonstrated by past space missions, e.g. Deep Impact and Hayabusa2 (A'Hearn et al., 2005; Saiki et al., 2013). For the purpose of our study, we use Hayabusa2's Small Carry-on Impactor (SCI) as the seismic source model. The SCI had a mass of 2 kg and was accelerated to a velocity of 2 km/s, yielding a nominal 8 MJ of kinetic energy upon impact. Since an impactor like SCI would be small relative to seismic wavelengths, we approximate it as a point source.

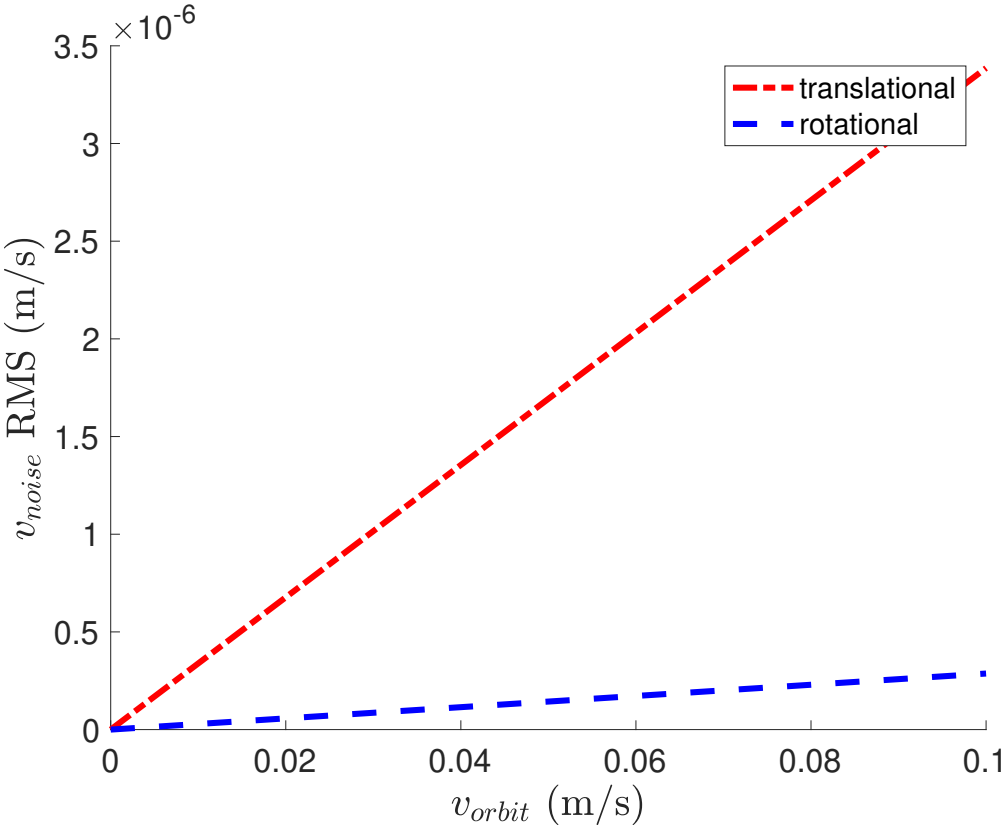


Figure 2.11: Simulated RMS velocity noise as a function of orbital velocity for an LDV positioned 2 km from an asteroid surface. The LDV has a 775 nm laser with a $1/e^2$ spot radius of 2.5 cm. The speckle noise is larger if the beam translates over the asteroid surface (red) than in the case where the beam rotates about a fixed point on the surface (blue).

Following Meschede et al. (2011), we describe an impact point force as,

$$\mathbf{f}(\mathbf{x}, t) = \hat{\mathbf{f}}\ p\ S(t)\delta(\mathbf{x} - \mathbf{x}_s), \tag{2.11}$$

where $p$ is the momentum of the impacting object, $S(t)$ is the source time function, $\delta$ is the delta function locating the impact at point $\mathbf{x}_s$, and $\hat{\mathbf{f}}$ is the direction of the impact relative to the surface normal. As suggested by Meschede et al. (2011), we assume that the source time function is a Gaussian,

$$S(t) = \sqrt{\frac{\pi}{\tau^2}} e^{\frac{-\pi^2 t^2}{\tau^2}}, \tag{2.12}$$

where $\tau$ is the halfwidth of the seismic pulse. For such Gaussian source time functions, the seismic energy is,

$$E_s(t) = \frac{F^2 \pi^{3/2}}{2^{5/2} \tau^3 \rho} \left( \frac{1}{3v_p^3} + \frac{2}{3v_s^3} \right), \tag{2.13}$$

where $F$ is the momentum of the impactor, $v_p$ and $v_s$ are the longitudinal and transverse wave velocities of the medium, respectively, and $\rho$ is the density of the target surface (Aki and Richards, 2002).

The time constant, $\tau$, is not well constrained (Meschede et al., 2011). We can estimate $\tau$ based on the seismic efficiency of the impact, $k$, which is defined as the ratio of kinetic energy transferred into seismic energy upon impact (Meschede et al., 2011),

$$k = \frac{E_s}{E_k}. \tag{2.14}$$

Laboratory testing indicates that large impacts in weak materials can have a seismic efficiency as little as $k \approx 10^{-5}$ (Moore et al., 1970), whereas smaller well coupled impacts or buried explosions can have a much higher seismic efficiency of up to $k \approx 10^{-2}$ (Gault, 1963; Titley, 1966). More recent studies combining laboratory measurements and numerical simulations suggest that the seismic efficiency of impacts can be constrained between $k \approx 10^{-5}$ and $k \approx 10^{-3}$ (Güldemeister and Wünnemann, 2017; Matsue et al., 2019). We use these values as a low and high bound for the seismic energy expected from an impactor. By estimating

the seismic energy in Equation 2.14 from the seismic efficiency and the impactor's kinetic energy, we can solve for $\tau$ using Equation 2.13, and then use Equation 2.12 to describe the source pulse.

As previously stated, we assume that the instrument records seismic signals on the opposite side of its target body for two reasons: 1) the instrument would record waves that travel through the center of the asteroid, and 2) the spacecraft would be safe from any debris from the impact. If we assume that the asteroid is a homogeneous medium, the vertical surface displacement from a longitudinal wave recorded on the opposite side of 101955 Bennu from an impact is

$$u^p(t) = \frac{1}{4\pi d_B \rho v_p^2} S\left(t - \frac{d_B}{v_p}\right), \tag{2.15}$$

where $d_B$ is the diameter of 101955 Bennu, and $S$ is the source time function, Equation 2.12 (Aki and Richards, 2002). By taking the derivative of Equation 2.15, we get the velocity of the surface at the LDV measurement location.

For an impactor analogous to Hayabusa2's SCI, we find seismic energy concentrated between 5 and 200 Hz. Significant uncertainty characterizes the seismic efficiency of an impact in asteroid regolith, so the ranges in the expected frequency and peak ground velocity (PGV) are large. Figure 2.12 illustrates a synthetic seismogram for an ideal impact source after propagating 500 m, about the radius of 101955 Bennu, in a homogeneous medium with $v_p = 450$ m/s. This velocity is consistent with estimated seismic velocities in the near surface lunar regolith (Heffels et al., 2017; Kovach and Watkins, 1973). For a high seismic efficiency case of $k = 10^{-3}$, a peak frequency of 60 Hz would be expected and a PGV of 0.1 mm/s would be possible. For the low seismic efficiency case of $k = 10^{-5}$, a peak frequency of 20 Hz would be expected and a PGV of 5 $\mu$m/s would be possible. In general, a smaller seismic efficiency leads to a lower amplitude and frequency, and a higher seismic efficiency leads to a higher amplitude frequency. We evaluate the ability to separate speckle noise from seismic signals based on the worst case seismic efficiency, $k = 10^{-5}$.

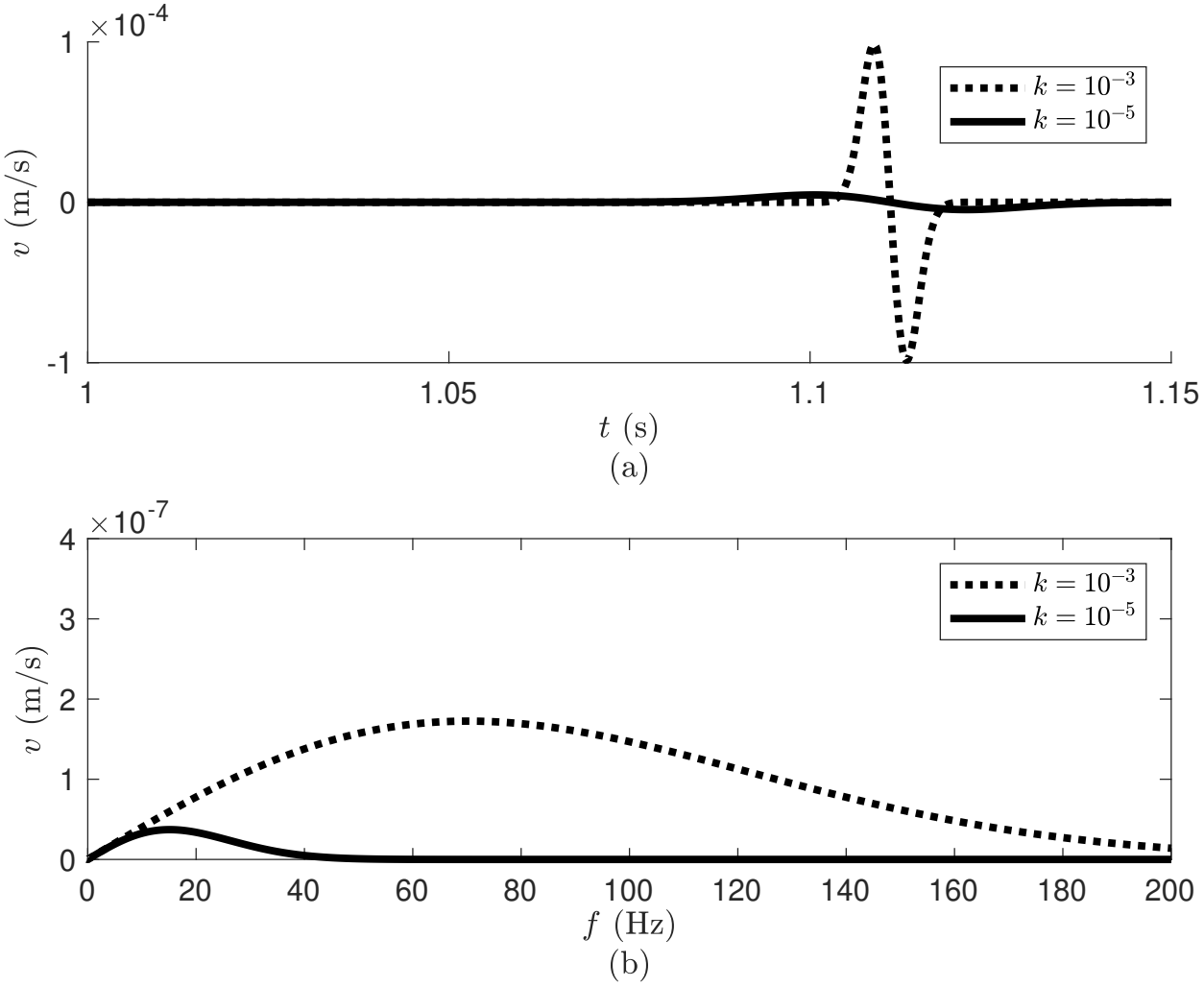


Figure 2.12: (a) The ground motion signals from an impact seismic source similar to the Hayabusa2 SCI after propagating 500 m in a 450 m/s velocity homogeneous model. The examples shown correspond to high efficiency $k = 10^{-3}$ and low efficiency $k = 10^{-5}$ impacts. (b) Illustrates the frequency spectrum of the seismic signals.

### 2.3.2 Seismic propagation through 101955 Bennu

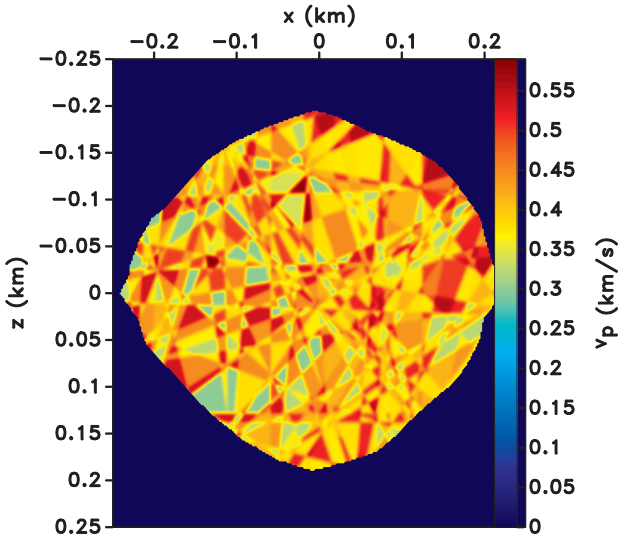


Figure 2.13: Rubble pile asteroid velocity model we use to simulate seismic signals.

Figure 2.12 provides an estimate of the peak ground velocity and frequency content due to an impact source, but does not adequately capture the complexity of true seismic signals. It is unlikely that a small asteroid like 101955 Bennu behaves as a homogeneous medium. The best interpretations from the OSIRIS-Rex mission suggest that 101955 Bennu is a rubble pile (Barnouin et al., 2019), likely dominated by boulders that are on the order of tens of meters in diameter (Scheeres et al., 2015), which is similar to typical seismic wavelengths. For scenarios where heterogeneities in the medium are on the same scale as seismic wavelengths, scattering theory or numerical simulations are necessary to create synthetic seismograms (Aki and Richards, 2002).

Figure 2.13 illustrates a conceptual rubble pile asteroid velocity model, consisting of angular blocks that represent impact shards that have gravitationally fallen together, as described by Asphaug (2008) and Scheeres et al. (2015). We assume that no large void spaces are present, or that they have been filled with regolith, which acts as a low seismic velocity medium. The compressional seismic wave velocity of asteroid materials is unknown; however, asteroid regolith likely has a similar velocity to regolith on the Moon. The near lunar surface

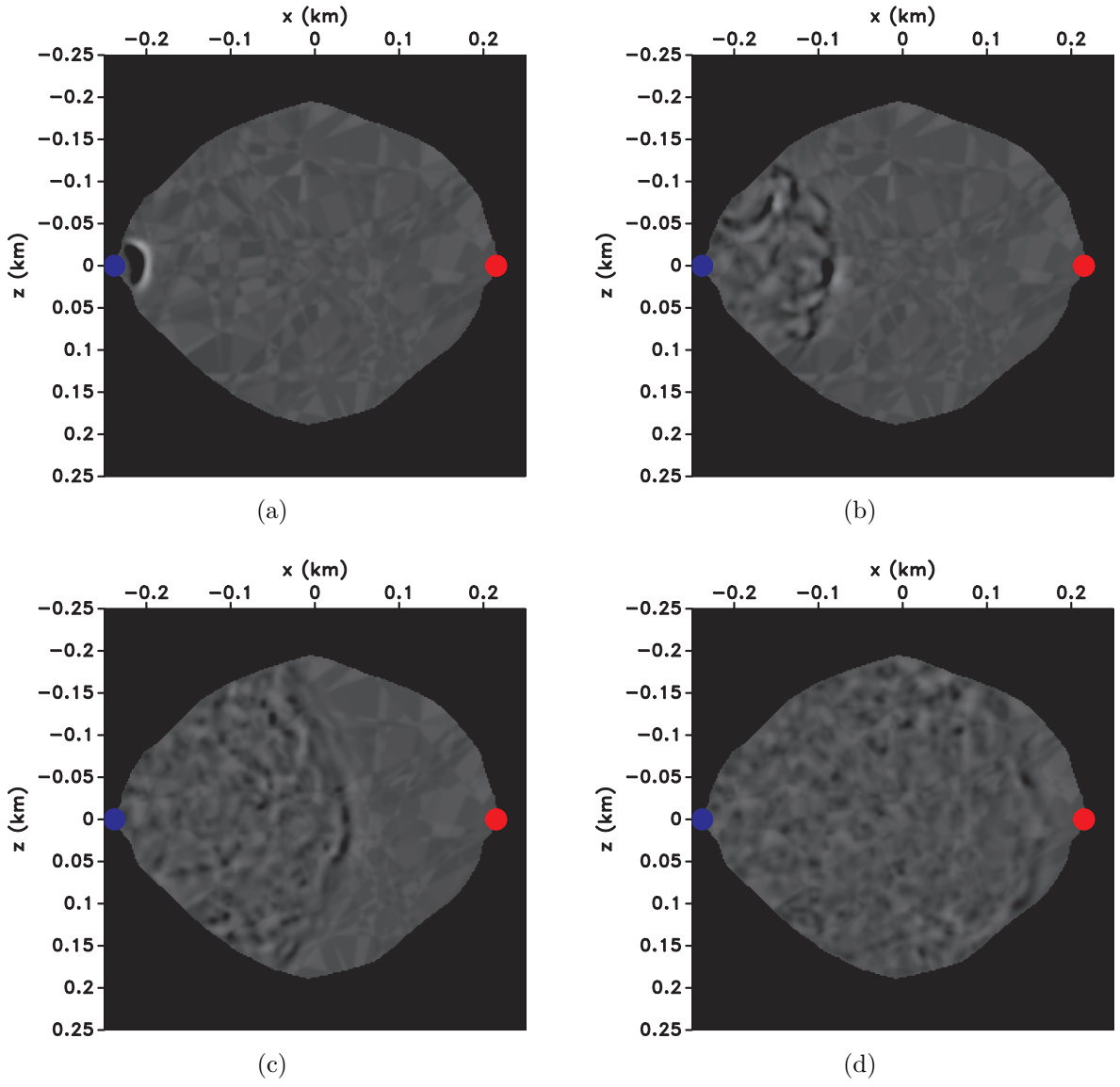


Figure 2.14: Wavefield snapshots from an impactor with an efficiency of $10^{-5}$ at $t = 0.15$ s, $t = 0.45$ s, $t = 0.75$ s, and $t = 1.05$ s after impact, respectively. The blue dot indicates the impact location, and the red dot indicates the LDV recording location.

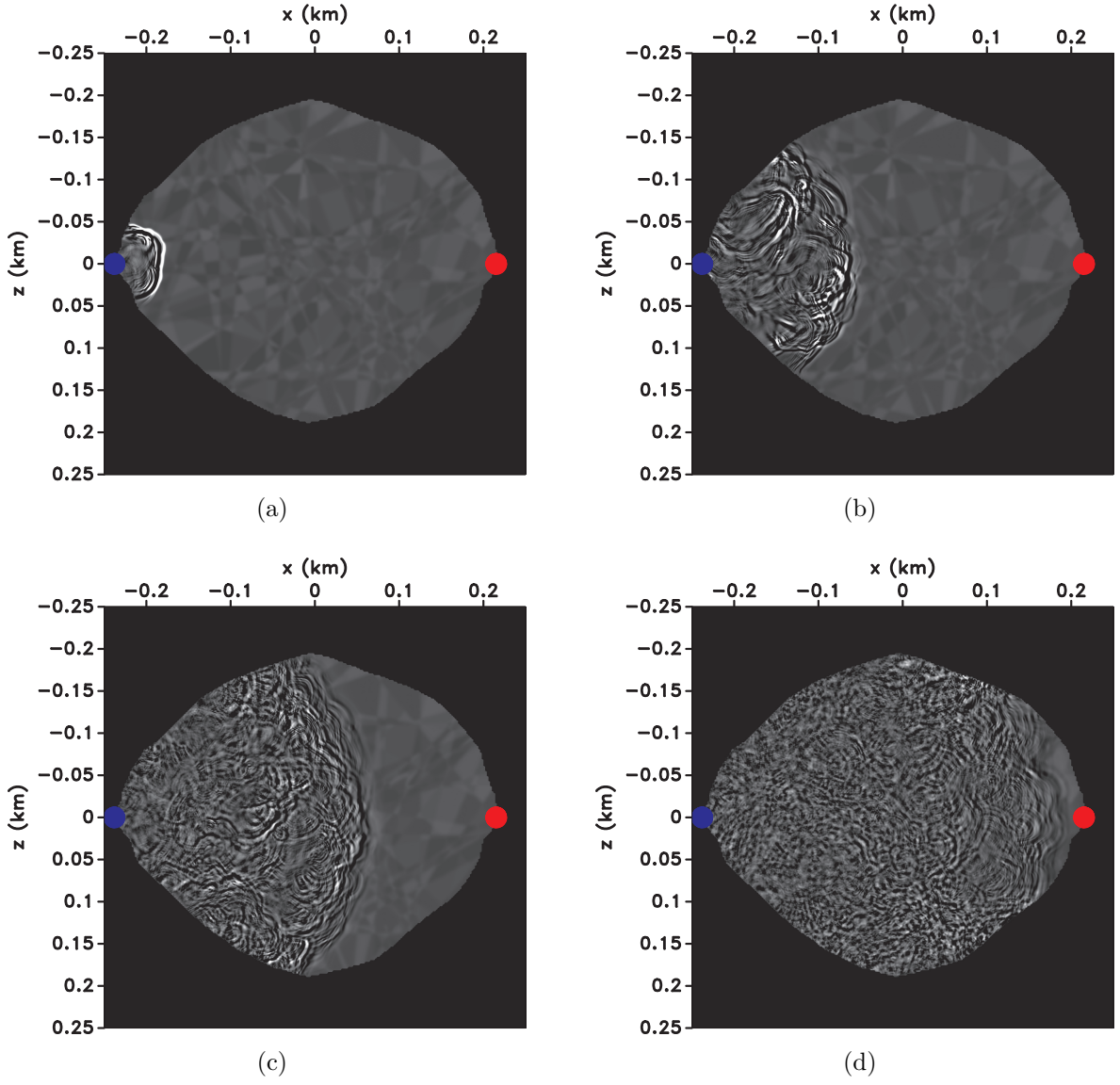


Figure 2.15: Wavefield snapshots from an impactor with an efficiency of $10^{-3}$ at at $t = 0.15$ s, $t = 0.45$ s, $t = 0.75$ s, and $t = 1.05$ s after impact respectively. The blue dot indicates the impact location, and the red dot indicates the LDV recording location.

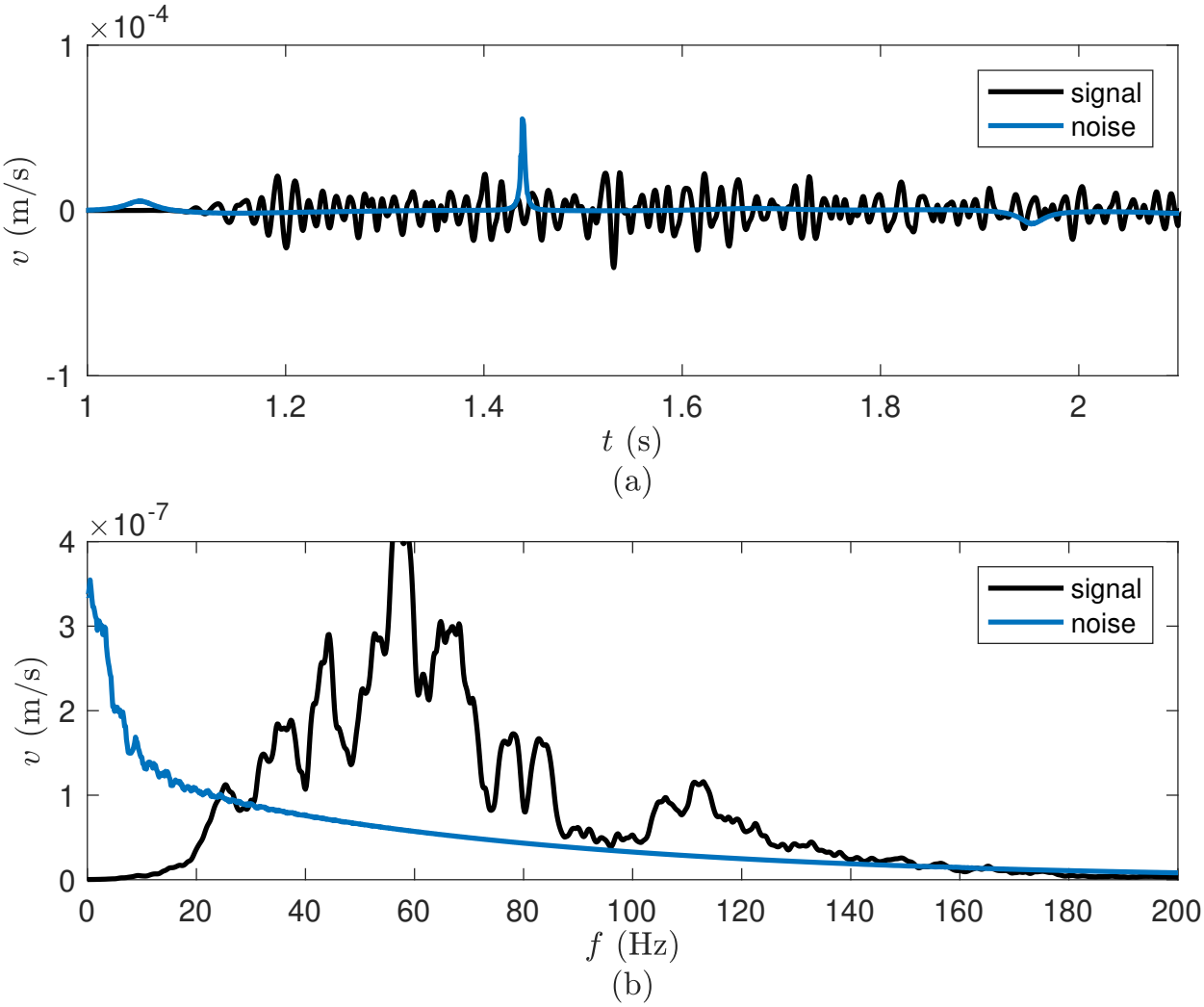


Figure 2.16: Comparison of a speckle noise trace from Figure 2.10 with a seismic trace from an impactor with an efficiency of $k = 10^{-3}$.

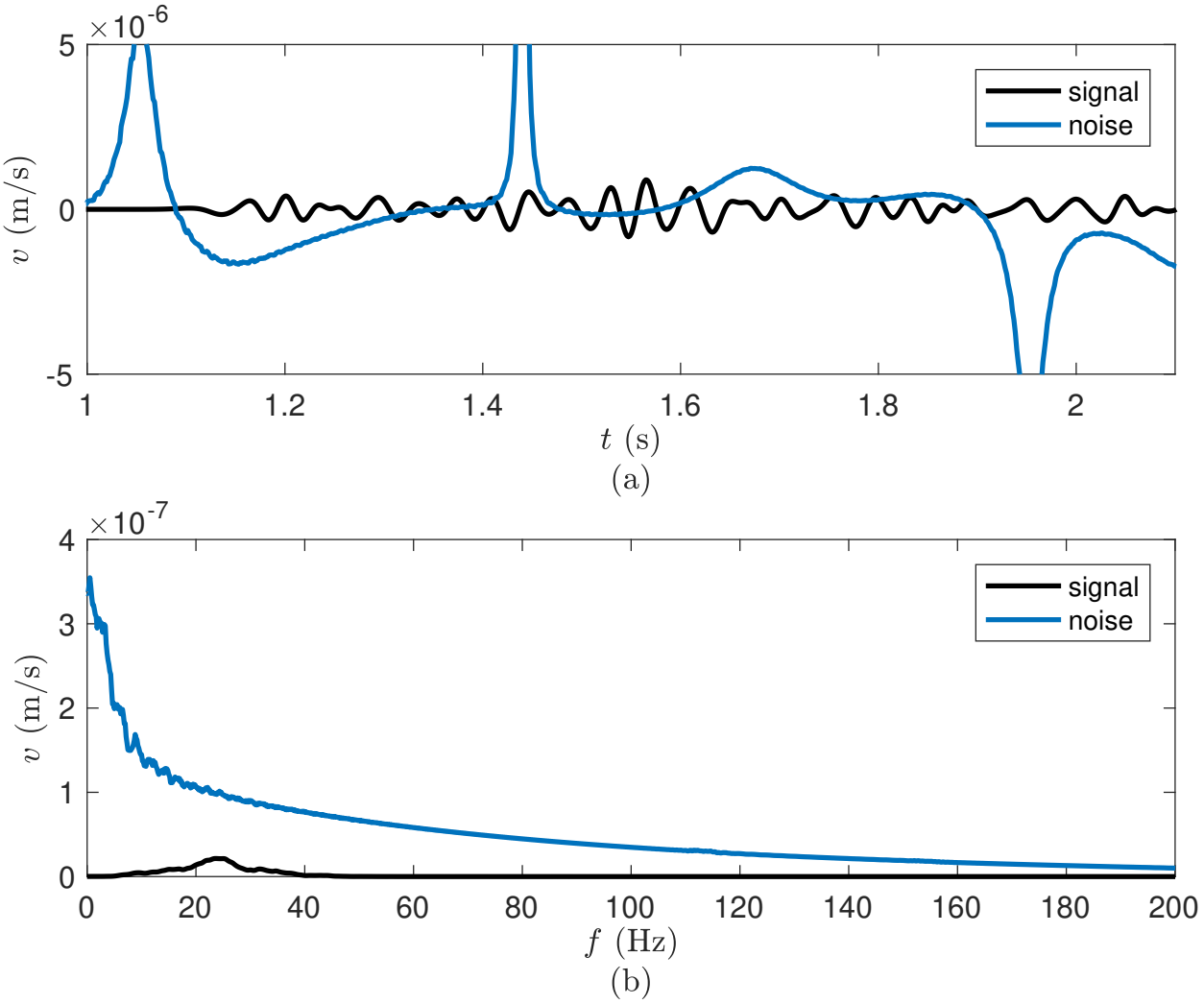


Figure 2.17: Comparison of a speckle noise trace from Figure 2.10 with a seismic trace from an impactor with an efficiency of $k = 10^{-5}$. Unlike the high seismic efficiency impact signal in Figure 2.16, the lower seismic efficiency impact produces a seismic signal with much lower amplitude than the speckle noise.

exhibits a compressional wave velocity of around 300 m/s and gradually increases with depth (Heffels et al., 2017; Kovach and Watkins, 1973). Per contra, laboratory measurements of carbonaceous meteorites suggest that intact asteroid fragments could have velocities as fast as 1-6 km/s (Jones, 2009). However, these measurements were made on centimeter sized samples with compressional waves in the MHz frequency range and may not be indicative of the bulk properties of asteroids at the seismic wavelength scale. Thus, for our rubble pile model, we assume velocities between 300 m/s to 600 m/s, which is consistent with estimated velocities in the near lunar surface. We simulate compressional wave propagation through the model using acoustic finite differences to generate a synthetic seismogram at a location on the opposite side of the asteroid from of the impact source. We also scale the synthetic seismogram by an exponentially decaying curve to approximate intrinsic attenuation using a seismic quality factor of $Q = 3000$, which is consistent with the low intrinsic attenuation observed in the lunar crust (Nakamura and Koyama, 1982).

Figures 2.14 and 2.15 illustrate wavefield snapshots for a low seismic efficiency $k = 10^{-5}$ impact, and a high seismic efficiency $k = 10^{-3}$ impact, respectively. The asteroid's heterogeneity leads to significant wavefield scattering within the interior of the body. Since the asteroid is surrounded by vacuum, the scattered waves cannot escape from the asteroid's interior, and continue to ring throughout the asteroid. Figure 2.16 and 2.17 display the resulting synthetic seismograms from the low and high seismic efficiency impact wavefield simulations, respectively (c.f. Figures 2.14 and 2.15). The wavefield scattering induced by the model heterogeneity reduces the PGV at the recording location as compared to the homogeneous propagation waveforms shown in Figure 2.12. The synthetic seismograms are consistent with other asteroid impact modeling studies (Richardson et al., 2005), which predict waveforms dominated by long-ringing coda from scattering.

Figures 2.16 and 2.17 also compare the synthetic seismograms with a speckle noise realization. Figure 2.16 shows that the high efficiency impact seismic signal, as simulated in Figure 2.15, has both greater magnitude and higher frequency content than the speckle

noise. This signal would adequately be separated by high-pass filtering. Figure 2.17 illustrates that the low efficiency impact signal has a lower magnitude than the speckle noise, and falls below the amplitude spectrum of the speckle noise at all frequencies. This is a challenging separation case since the noise has more power than the signal. We seek methods that attenuate the speckle noise, while boosting the power of the seismic signal. To address the seismic signal and speckle noise separation problem, we average multiple signals as suggested by Dräbenstedt (2014). To further reduce speckle noise, we exploit the separation of the seismic signal from speckle noise in the frequency domain.

## 2.4 Seismic signal separation from speckle noise

### 2.4.1 Signal diversity

The ratio of seismic signal power to speckle noise power can be increased through signal diversity combining. Diversity combining involves recording multiple measurements of the same signal and combining them to reduce the incoherent noise while boosting the coherent signal. The method relies on the fact that all measurements record independent speckle noise, but have the same underlying ground velocity signal. A single LDV can record multiple simultaneous ground velocity measurements by using multiple detectors that exploit polarization and spatial diversity in the reflected speckle pattern (Dräbenstedt, 2014). Polarization diversity refers to the fact that orthogonal polarizations of the speckle pattern are independent. Thus, an LDV with two co-located detectors that record orthogonal polarization of light could record two simultaneous measurements that have independent speckle noise. Dräbenstedt (2014) and Rembe et al. (2015) have successfully exploited polarization diversity in order to combine two signals. In order to combine more than two simultaneous measurements, we propose exploiting spatial diversity using an LDV with multiple detectors at separate spatial locations in the reflected speckle field. Figure 2.18 illustrates potential multiple detector layout options that allow for different portions of the speckle pattern to be sampled. The speckle noise observed by any two detectors separated in space would be uncorrelated as long as the detector's centers are placed more than an average speckle

diameter apart, as quantified in Equation 2.10 (Rothberg et al., 2004).

### 2.4.2 Maximal ratio combining

There are different ways to combine signals that contain a common signal, but have independent noise. Dräbenstedt (2014) and Rembe et al. (2015) demonstrate signal diversity combining of two LDV signals via Maximal Ratio Combining (MRC). This method takes a weighted average at each time step of the observations using weights that maximize the signal to noise ratio (SNR). Mathematically, the $i^{th}$ signal, $s_i$, can be expressed as,

$$s_i(t) = v(t) + n_i(t) \tag{2.16}$$

where $n_i(t)$ is the speckle noise unique for the $i^{th}$ detector, $v(t)$ is the surface velocity signal, and $t$ is time. Using the method described by Dräbenstedt (2014) and (Rembe et al., 2015), an approximation of the ground velocity signal $\tilde{v}(t)$ can be achieved using a weighted sum of the signals,

$$\tilde{v}(t) = \sum_{i=1}^{n} w_i(t) s_i(t) \tag{2.17}$$

The weights $w$ should be chosen such that the variance of the resulting signal is minimized. Dräbenstedt (2014) demonstrates that the weights that satisfy this goal are given by

$$w_i(t) = \left[ \sum_{j=1}^{n} \frac{\sigma_i^2(t)}{\sigma_j^2(t)} \right]^{-1} \tag{2.18}$$

where $\sigma_i^2$ is the variance of the signal $\mathbf{s}_i$ from the ground velocity signal. The variance of each signal, $\sigma_i^2$, is unknown; however, Dräbenstedt (2014) shows that the variance of the speckle noise is inversely proportional to the total light intensity on the $i^{th}$ detector. Thus, the relative variance, $\sigma_i^2/\sigma_j^2$, between any two detectors with indices $i$ and $j$ is known. The relation between the velocity signal's variance and signal intensity is apparent in Figure 2.9, where the large speckle noise spikes correlate with low signal intensity.

The weighted average solution in Equation 2.17 can be rewritten in matrix notation relating the signal from each LDV detector with the true ground velocity signal. Since

we know that each signal recorded by a different detector has the same underlying ground velocity signal, we can write,

$$\mathbf{d} = \mathbf{I}\mathbf{v}, \tag{2.19}$$

where $\mathbf{v}$ is a column vector of the true ground velocity signal $v(t)$, $\mathbf{I}$ is an $M$-high stack of $N \times N$ identity matrices, and $\mathbf{d}$ is a column vector of the signal recorded by each detector stacked on top of each other,

$$\mathbf{d} = [\mathbf{s}_1\ \mathbf{s}_2\ ...\ \mathbf{s}_M]^T. \tag{2.20}$$

In this formulation, $N$ is the length of each signal, $M$ is the number of detectors, and the vectors $\mathbf{s}_i$ represent time series of the velocity signals $s_i(t)$ recorded by each LDV detector. In the ideal case with no noise, as represented by Equation 2.19, each recorded signal vector $\mathbf{s}_i$ is a copy of the true ground motion signal vector, $\mathbf{v}$.

To solve for an approximation of the ground velocity $\tilde{\mathbf{v}}$ when given a data vector $\mathbf{d}$ contaminated with speckle noise, we solve a weighted least squares objective function,

$$\tilde{\mathbf{v}} = argmin_{\mathbf{v}}||\mathbf{W}(\mathbf{d} - \mathbf{I}\mathbf{v})||^2 \tag{2.21}$$

where $\mathbf{W}$ is the weighting matrix, given by a diagonalization of the weights from Equation 2.18. Explicitly,

$$\mathbf{W} = \text{diag}([w_{11}\ w_{12}\ ...\ w_{MN}]), \tag{2.22}$$

where $w_{ij}$ is the weight for the $i^{th}$ receiver at the $j^{th}$ time index.

Solving Equation 2.21 produces the same result as the weighted average solution in Equation 2.17. The benefit of the matrix formulation is that we can modify it in order to take advantage of the signal characteristics. The next section describes how we use this formulation to impose structure on the recovered signal by exploiting the separation of the seismic signal and the speckle noise in the frequency domain.

### 2.4.3 Signal fitting model

Figure 2.17 suggests that the seismic signal is concentrated in a narrow bandwidth. Thus, we assume that the true ground velocity signal $\mathbf{v}$ can be expressed by a band-limited subspace model,

$$\mathbf{v} = \mathbf{S}\mathbf{m}, \tag{2.23}$$

where $\mathbf{S}$ is the operator matrix that transforms a set of band-limited subspace model coefficients, $\mathbf{m}$, into a time domain signal. In this case, $\mathbf{S}$ is a tall matrix, meaning that $\mathbf{m}$ has fewer coefficients than $\mathbf{v}$.

We use Discrete Prolate Spheroidal Sequences (DPSS) to create band-limited subspaces because the sequences provide an efficient basis for sampled band-limited signals (Davenport and Wakin, 2012). For a given signal length of $N$ samples and a bandwidth of $\beta$ Hz, the first DPSS is the unique length $N$ sequence that has maximum energy concentration within the band $[-\beta/2, \beta/2]$. The second DPSS is the sequence that is most energy concentrated in that band while also being orthogonal to the first vector. The third DPSS is the next most concentrated sequence in the band while being orthogonal to both the first and second sequences, and so on. Given a sampling frequency of $F_s$, the first $NF_s\beta - 1$ DPSS vectors have near complete energy concentration within the band $[-\beta/2, \beta/2]$. Any sequences after the $NF_s\beta - 1$ sequence have near zero energy within the band $[-\beta/2, \beta/2]$. Thus, the first $NF_s\beta - 1$ DPSS vectors form an ideal basis for a band-limited subspace spanning $[-\beta/2, \beta/2]$. A full derivation of DPSSs can be found in Slepian and Pollak (1961) and Landau and Pollak (1961), and a more recent summary and application is available in Davenport and Wakin (2012).

Since we can estimate the bandwidth of the expected seismic signal based on impactor modeling, we can estimate a center frequency $f_c$ and a bandwidth $\beta$ to construct a DPSS transform matrix. However, by definition, DPSSs are centered around zero frequency, such that the sequences provide support for all frequencies in the range $-\beta/2$ to $\beta/2$. To create

a band-limited subspace centered around a frequency $f_c$, we modulate all sequences by $f_c$, as described in Davenport and Wakin (2012),

$$\mathbf{S} = e^{i2\pi f_c t}\mathbf{S}_0, \tag{2.24}$$

where, $\mathbf{S}_0$ is the zero center set of DPSSs that satisfy the given bandwidth $\beta$. The result, $\mathbf{S}$, denotes the operator that transforms coefficients of band-limited DPSS vectors centered at a frequency $f_c$ to a time domain signal. Figure 2.19 illustrates how well the seismic trace in Figure 2.17 is approximated by different bandwidths. For example, an approximation of over 20 dB can be achieved with a subspace spanning a bandwidth of 50 Hz centered around 30 Hz.

As previously stated, each LDV detector records the same ground velocity. Thus, each signal should be related to the same band-limited subspace coefficients. Using this knowledge, we relate the recorded signals, $\mathbf{d}$, to a set of coefficients, $\mathbf{m}$, in the band-limited subspace with the operator $\mathbf{G}$,

$$\mathbf{d} = \mathbf{G}\mathbf{m}, \tag{2.25}$$

where $\mathbf{G}$ is an M-high stack of $\mathbf{S}$ matrices,

$$\mathbf{G} = [\mathbf{S}\ \mathbf{S}\ ...\ \mathbf{S}]^T. \tag{2.26}$$

We solve a modified inverse problem by finding $\tilde{\mathbf{m}}$ such that,

$$\tilde{\mathbf{m}} = argmin_{\mathbf{m}}||\mathbf{W}(\mathbf{d} - \mathbf{G}\mathbf{m})||^2. \tag{2.27}$$

Using conventional inverse theory, the weighted least squares solution to Equation 2.27 (Tarantola, 2005) is,

$$\tilde{\mathbf{m}} = (\mathbf{G^T}\mathbf{W^T}\mathbf{W}\mathbf{G})^{-1}\mathbf{G^T}\mathbf{W^T}\mathbf{W}\mathbf{d}, \tag{2.28}$$

where the weighting matrix is the same as Equation 2.22. Finally, the time domain seismic signal is recovered by,

$$\tilde{\mathbf{v}} = \mathbf{S}\tilde{\mathbf{m}}. \tag{2.29}$$

We note that the seismic impulses we consider are not perfectly band-limited. Thus, a band-limited subspace cannot fully recreate the seismic signal, as demonstrated in Figure 2.19. In the imaginary scenario where we know the true seismic signal $\mathbf{v}$, we can find the optimal signal recovery by the projection of $\mathbf{v}$ onto the subspace spanned by $\mathbf{S}$. From Moon and Stirling (2000), this is given by,

$$\tilde{\mathbf{v}}_{opt} = \mathbf{S}(\mathbf{S^T S})^{-1}(\mathbf{S^T v}). \tag{2.30}$$

The best SNR achievable using our algorithm is therefore the ratio of the power of $\mathbf{v}$ and $(\tilde{\mathbf{v}}_{opt} - \mathbf{v})$. Regardless of how many signals are combined, $\tilde{\mathbf{v}}$ will never provide a more accurate solution than $\tilde{\mathbf{v}}_{opt}$. Thus, the goal of our algorithm is to converge to $\tilde{\mathbf{v}}_{opt}$ with as few detectors as possible.

Figure 2.20 illustrates the efficacy of our signal diversity combining algorithm by removing the speckle noise from the low efficiency impact seismic trace in Figure 2.17 using a 7-53 Hz subspace approximation. An improvement of 10 dB to the SNR is achieved after combining two signals, and a further 10 dB is obtained upon combining 14 signals. Figure 2.21 illustrates the SNR of the recovered signal in dB using our algorithm as a function of the number of independent signals recorded. The figure also shows the effect of using different bandwidths for signal separation. As more signals are added, the SNR approaches the ideal value, which is specific for each band-limited approximation. The more narrow the band, the lower the ideal approximation SNR, but the faster the convergence to that SNR. All band-limited cases achieve higher SNRs than the weighted average approach, as proposed by Dräbenstedt (2014), provided an adequate bandwidth is chosen. Regardless of what combining method is used, there is diminishing return for each new signal combined. The combining of an additional signal does not guarantee SNR improvement because some speckle noise traces may have more large spikes over the time region of interest than others; however, on average the SNR improves with additional receivers. Figure 2.21 illustrates SNR improvement curves from the average of 20 simulations. The uncertainty bars highlight the variability in improvement as a result of variability in the individual speckle noise traces.

Lastly, we demonstrate the recovery SNR as a function of PGV. The recovery of the seismic signal largely depends on the ratio in magnitude between the seismic signal and the speckle noise. To demonstrate how well we can separate the signals, we consider seismic signals with a range of PGV values. Using the high efficiency signal from Figure 2.16, we simulate separation from speckle noise with its PGV scaled with a range of values between $10^{-5}$ m/s and $10^{-8}$ m/s. Figure 2.22 illustrates that as the PGV increases, the recovery improves. We can push the possible signal recovery down to $10^{-8}$ m/s PGV with the inclusion of 14 detectors and our combining algorithm.

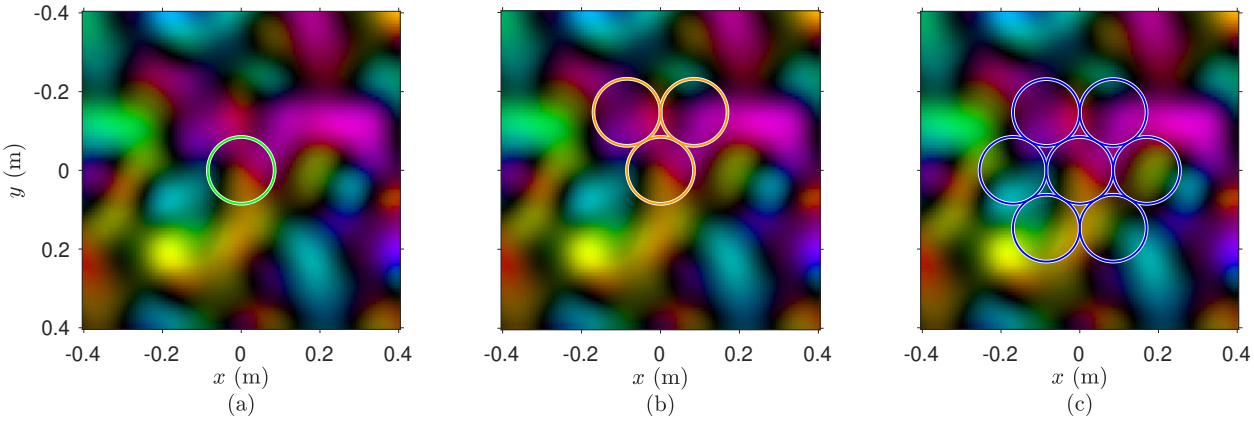


Figure 2.18: LDV detector arrangements capable of recording multiple signals: (a) represents 1 detector recording 2 signals of orthogonal polarization, (b) 3 detectors recording 6 signals, and (c) 7 detectors recording 14 signals. Each detector is roughly the same size as the speckles in order to record independent speckle noise.

## 2.5 Discussion

Creating a detailed image of the interior of comets and asteroids is of high priority for the planetary science community (Asphaug, 2009; Binzel et al., 2010; Scheeres et al., 2015). To accomplish this, missions are routinely proposed using radar or seismic theory to probe small body interiors (Asphaug et al., 2014; Grimm et al., 2015; Plescia et al., 2018; Sava et al., 2015). However, radar imaging may only be viable in icy bodies that are nearly transparent to radar waves, and conventional seismic imaging may be prohibitively expensive and too technologically challenging to implement because multiple landed seismometers would

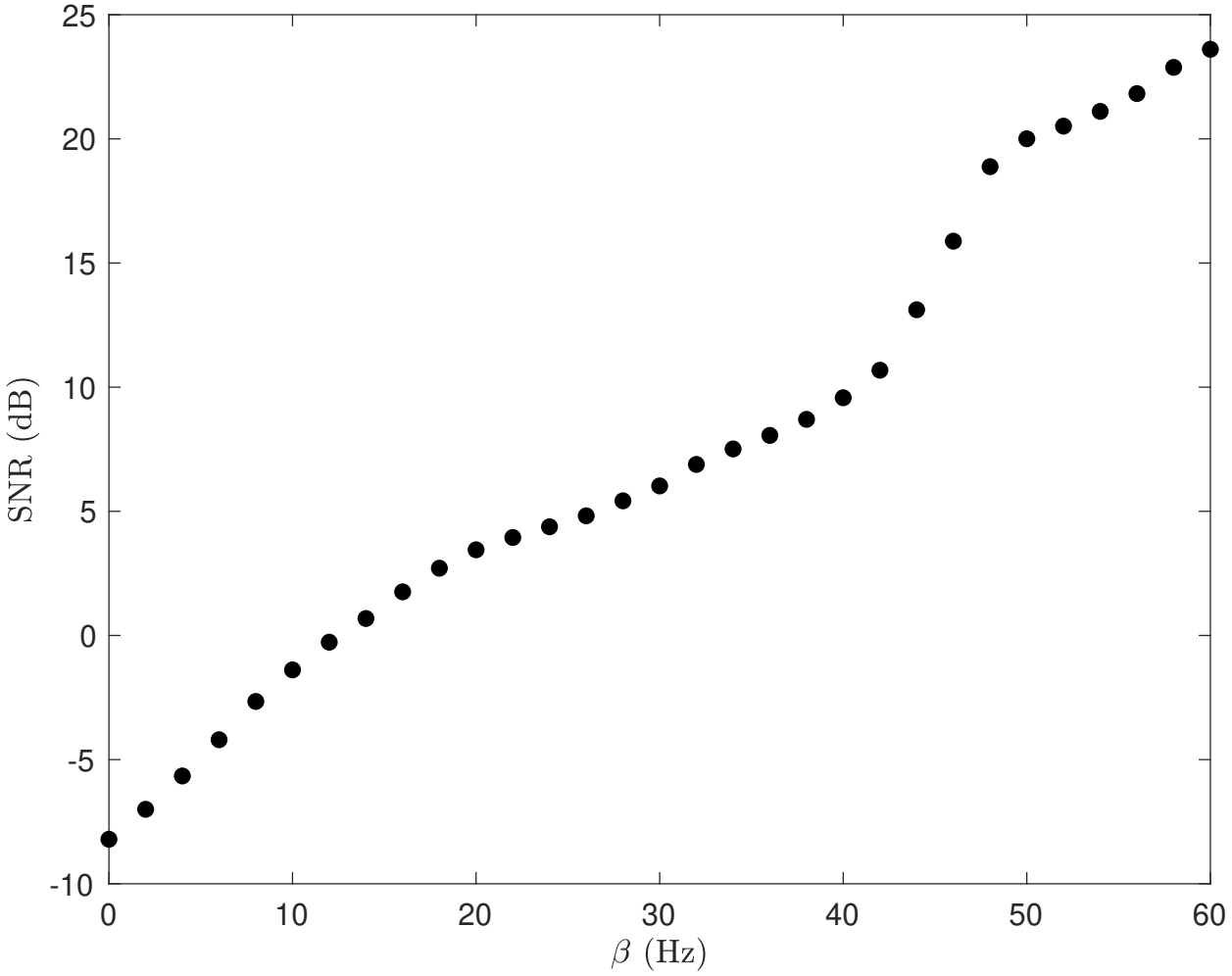


Figure 2.19: Signal-to-noise ratio of the approximation of the seismic trace in Figure 2.17 as a function of DPSS subspace bandwidth. The band is centered at 30 Hz, so a bandwidth of 15 Hz corresponds to a DPSS subspace that spans 15-45 Hz. The seismic signal can be well approximated using a narrow bandwidth.

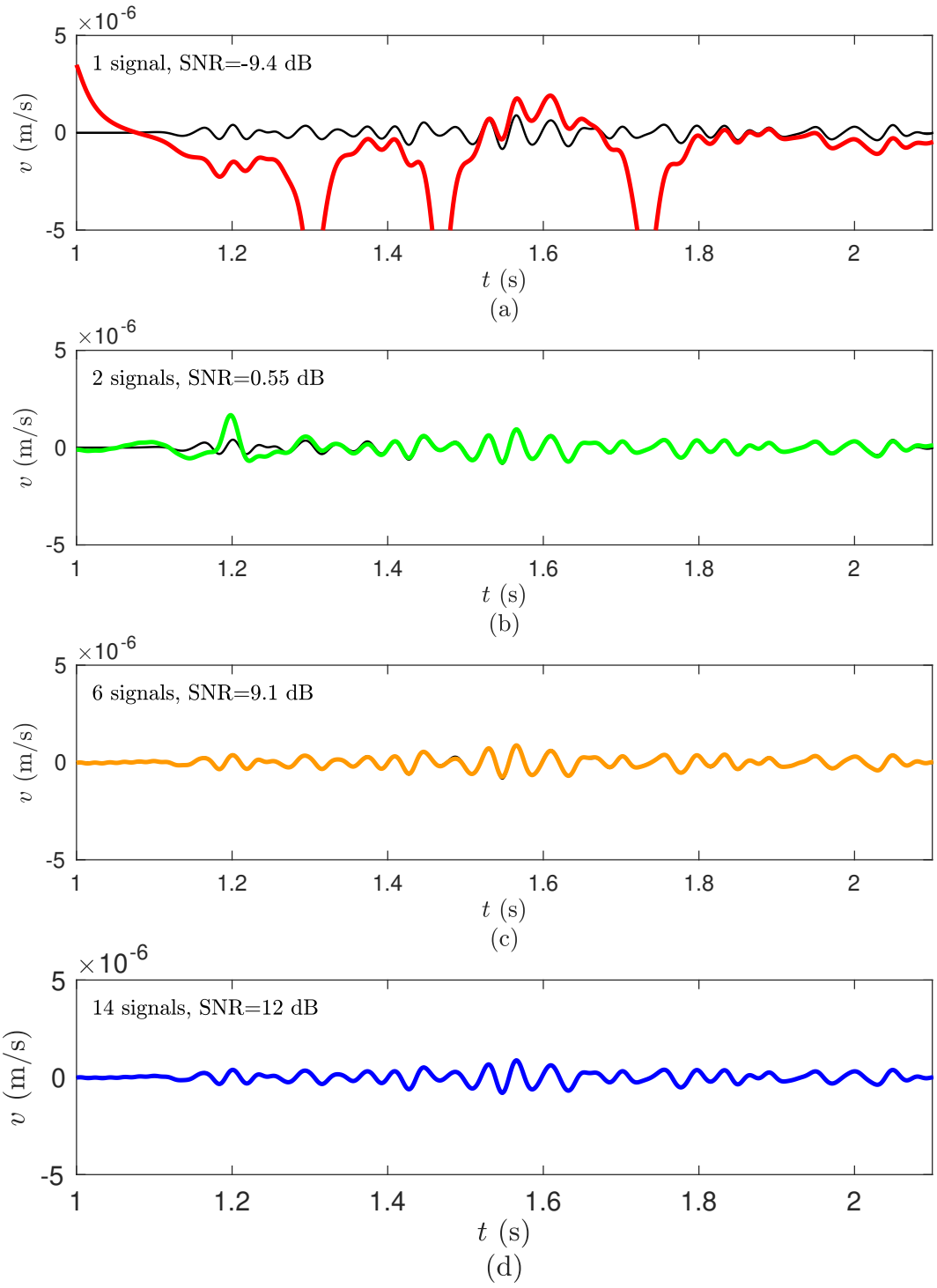


Figure 2.20: Recovered signal after combining multiple data traces that contain the same seismic signal and similar speckle noise as in Figure 2.17. (a) One LDV signal without any filtering; (b) combination two signals; (c) combination of six signals; (d) combination of 14 signals. Combining multiple signals significantly reduces speckle noise.

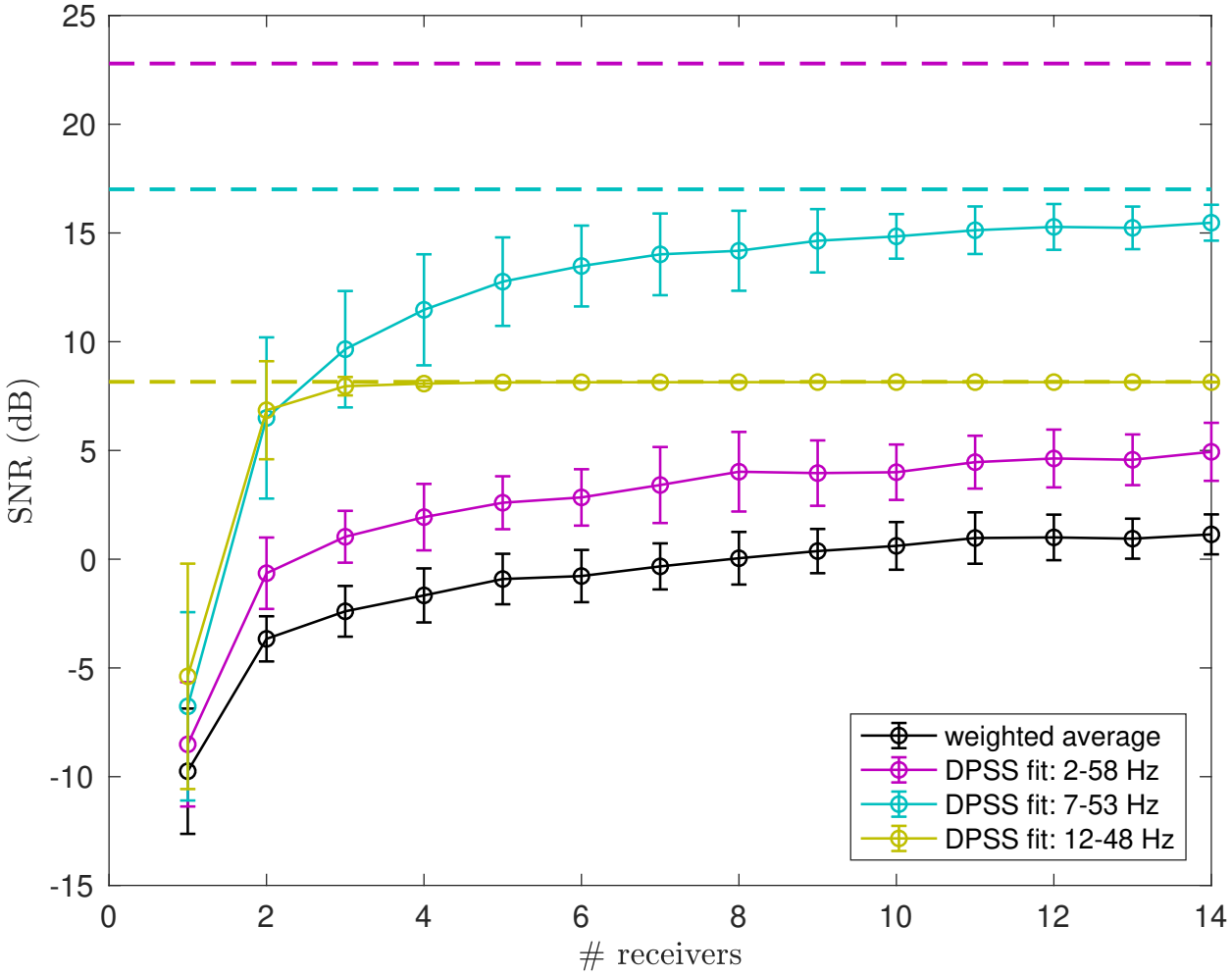


Figure 2.21: Signal improvement as a function of the number of signals combined. Each curve indicates the average of 20 simulations, and the uncertainty bars represent the standard deviation of the simulations. Black illustrates the weighted average approach, yellow illustrates the case using a narrow band to approximate the signal; magenta illustrates the case using a wide band for approximation, and cyan demonstrates a case using an optimal frequency band.

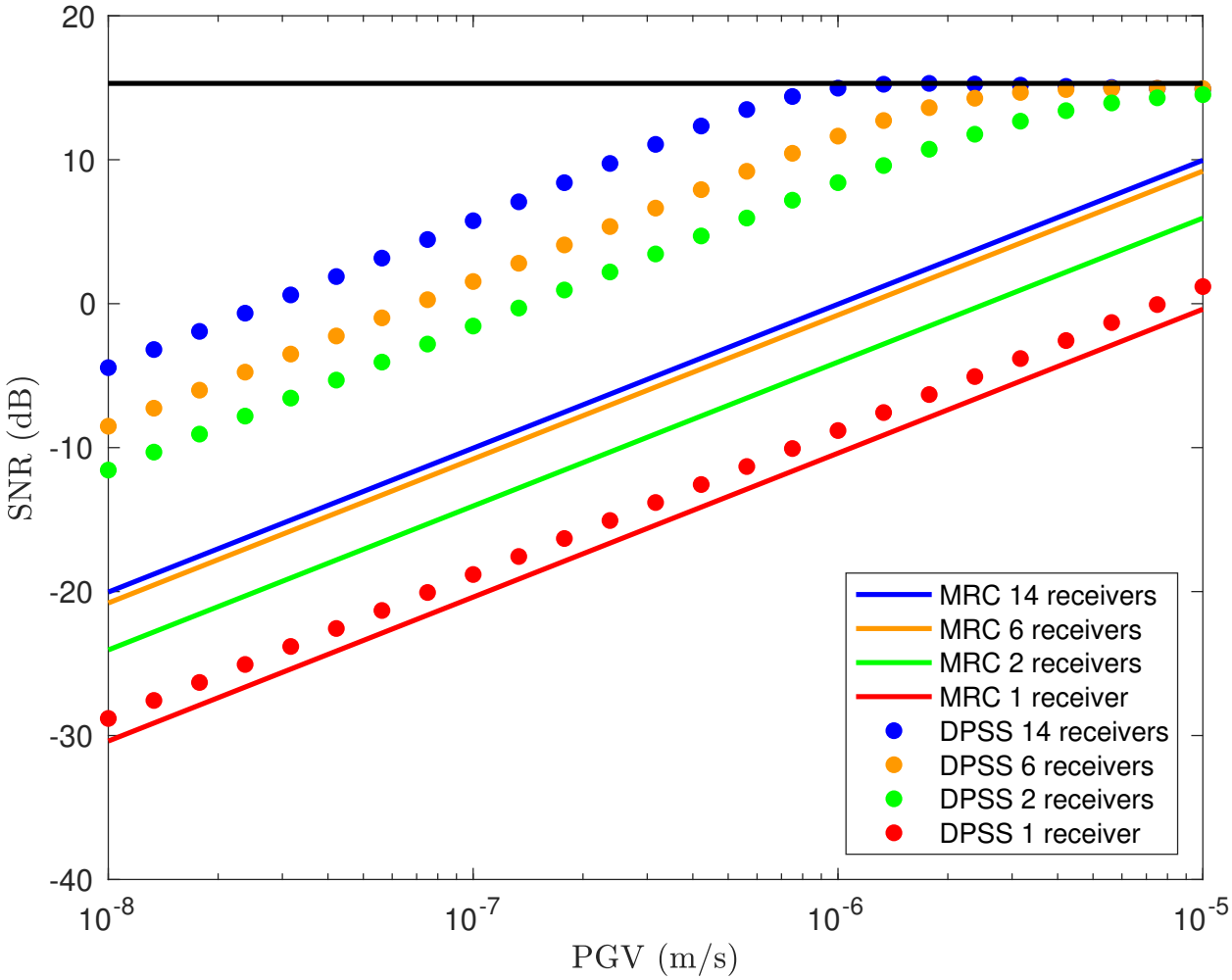


Figure 2.22: Signal recovery as a function of the peak ground velocity of the seismic signal. The signal used for testing is the same as shown in Figure 2.17, but scaled by different peak ground velocities ranging from $10^{-5}$ to $10^{-8}$ m/s. The dots indicate separation with a DPSS fit within 7 to 53 Hz, and the lines indicate separation with the weighted average approach. Red represents the SNR from 1 receiver, green the SNR after combining 2 signals, yellow the SNR after combining 6 signals, and blue, the SNR after combining 14 signals. The black line indicates the optimal signal approximation using the chosen bandwidth.

be needed. The seismic imaging instrument concept proposed by Sava and Asphaug (2019) seeks to alleviate these concerns by employing orbital LDVs as remote sensing seismometers. An orbital seismometer could obtain global seismic coverage of a small body and ultimately create a detailed image of its interior by using seismic migration and tomography techniques Sava and Asphaug (2019). However, global seismic data coverage with an LDV is contingent on the LDV's ability to record seismic data anywhere on a rough asteroid surface. Our results provide support to the concept by demonstrating that we can separate surface roughness induced laser speckle noise from seismic signals recorded by an orbital laser Doppler vibrometer. By demonstrating that an LDV can theoretically record a seismic signal on a natural rough small body surface, our work supports the development of low-cost direct observations of small body interior properties via orbital laser Doppler vibrometry.

Following an orbital acquisition scenario at the asteroid 101955 Bennu (Figure 2.1), we demonstrate in Figure 2.22 that speckle noise is a minor issue for strong seismic shaking scenarios of more than $10^{-5}$ m/s PGV, and can be reduced through signal diversity combining for light seismic shaking scenarios of less than $10^{-5}$ m/s PGV. Our work shows that signal recovery can be achieved for signals with a PGV down to $10^{-8}$ m/s by assuming frequency bandwidth properties of the seismic signal, and combining multiple independent LDV measurements. In general, we demonstrate that the laser speckle noise observed by an LDV laser incident on a rough surface can be quantified and removed. Our simulation method allows for the speckle noise to be determined for any orbital acquisition scenario defined by orbital velocity, distance from surface, and laser properties (c.f. Figure 2.11). We demonstrate that speckle noise can be combated with accurate spacecraft pointing, as demonstrated in Figure 2.11, and with the combination of more LDV detectors, as demonstrated in Figure 2.22. Thus, speckle noise attenuation in orbital vibrometry can be applied to other orbital scenarios provided a suitable balance of seismic source energy, spacecraft pointing, and number of LDV receivers is achieved.

## 2.6 Conclusion

In the broader effort to enable orbital seismology of small planetary bodies such as asteroids and comets, we demonstrate how to attenuate surface roughness induced laser speckle noise in laser Doppler vibrometer measurements. Specifically, we demonstrate: (1) how to quantify laser speckle noise in laser Doppler vibrometer measurements on distant rough surfaces, (2) how to quantify seismic signals from artificial impacts, and (3) how to separate seismic signals from speckle noise. We demonstrate these concepts with numerical simulations of an orbital LDV collecting seismic data transmitted through the asteroid 101955 Bennu from an artificial impact source; however, the methods we show apply for any LDV data acquisition on a rough surface. We demonstrate that laser speckle noise can be reduced in two ways, (1) accurate spacecraft pointing, and (2) through signal diversity combining. Our work shows that, even under worst case conditions, an accurate seismic signal can be recovered in spite of LDV speckle noise while in orbit over a rough asteroid or comet surface.

This result has broader implications for the future exploration of asteroid and comet interiors. Sava and Asphaug (2019) demonstrate that orbital laser Doppler vibrometry is a promising technique to remotely record seismic measurements on an asteroid or comet in order to create a detailed image of its interior, assuming that an LDV can provide an accurate measurement of ground motion on an unprepared asteroid or comet surface. This work provides a fundamental stepping stone toward achieving seismic imaging of small bodies by demonstrating that we can separate surface roughness induced laser speckle noise from seismic signals in simulated orbital LDV measurements.

## 2.7 Acknowledgments

This work was supported by the NASA Planetary Instrument Concepts for the Advancement of Solar System Observations (PICASSO) program (NNH16ZDA001N). The Center for Wave Phenomena at Colorado School of Mines provided logistic and computational support. The reproducible numeric examples in this paper use the Madagascar open-source software

package freely available from http://www.ahay.org (Fomel et al., 2013).

# CHAPTER 3

# CONCLUSIONS

Laser speckle noise is the dominant noise source when recording vibrations on a rough surface with a moving laser Doppler vibrometer Rembe et al. (2015). In this thesis, I demonstrate how to quantify and remove laser speckle noise from LDV measurements of seismic signals. In order to solve this research problem, I combine three fields of study: laser physics, seismology, and signal processing. In Chapter 2.2, I use principles of laser physics to describe the source of laser speckle noise. I use numerical simulations to quantify the noise for an orbital LDV scenario over the asteroid 101955 Bennu. In Chapter 2.3, I use seismological principles to describe the seismic signal produced from a small artificial impact. I simulate an impact scenario that correspond to a feasible scenario with current technology. Having described the speckle noise and seismic signal we expect for an orbiter around 101955 Bennu, in Chapter 2.4, I use signal processing techniques to separate the two signals. I demonstrate that it is possible to reduce speckle noise through signal diversity combining and subspace fitting. The reduction of speckle noise through these methods would allow an orbital LDV to record seismic measurements on a natural asteroid surface.

My study of the effect of speckle noise in orbital laser vibrometry significantly advances our understanding of how to design a functional instrument to record seismic data remotely over small bodies. My work expands the work of Sava and Asphaug (2019) by demonstrating an orbital laser vibrometer could function on an unprepared and naturally rough asteroid surface through the separation of seismic signals from speckle noise. This research the argument that an orbital laser vibrometer can obtain global seismological coverage of an asteroid or comet. The ability to record seismic measurements globally over an asteroid enables 3D seismic imaging, with which one could test asteroid interior structure hypotheses.

My work also expands upon the research of Dräbenstedt (2014) and Rembe et al. (2015). I provide a methodology to enhance the separation of speckle noise from object motion signals by exploiting a-priori knowledge of the signal. I also provide a theoretical demonstration of the performance of a multi-detector LDV. Although I have framed my research in terms of orbital seismology over asteroids, there is potential to apply my methodology toward conventional terrestrial LDV applications. Potential applications include: vibration sensing from moving platforms such as drones or vehicles, rotating component testing, or long distance structural monitoring laser beams affected by atmospheric scattering. All of these are scenarios where the light returning to the LDV might be deformed by scattering effects, and would be susceptible to speckle noise.

## 3.1 Future work

I demonstrate speckle noise reduction for an acquisition scenario at the small asteroid, 101955 Bennu. Can an orbital LDV be scaled to function on a larger body? The velocity of a spacecraft orbiting an asteroid increases with the mass of the asteroid, so I expect speckle noise that is higher in magnitude at larger bodies (c.f. Figure 2.11). Also, assuming the same impact source, the seismic signals would be smaller at a large body due to geometrical spreading as accounted for in Equation 2.15. However, this thesis demonstrates that speckle noise can be combated with accurate spacecraft pointing, as demonstrated in Figure 2.11, and with the combination of more LDV detectors, as demonstrated in Figure 2.22. Additionally, to increase the seismic signal strength, a more energetic impact source could be designed. Thus, I suggest that orbital vibrometry can be applied to larger bodies, provided a suitable balance of seismic source energy, spacecraft pointing, and number of LDV receivers is achieved. An exception to this argument is the distance at which an LDV must be from the surface for a safe orbit. In this thesis, I assume an orbit of 2 km above the surface. This distance is feasible for a spacecraft at a small asteroid (Daly et al., 2017) and is nearly within measurement range of some commercially available LDVs (Dräbenstedt et al., 2012; Lutzmann et al., 2011). If an LDV were to be used at a larger asteroid, it is likely that

its distance from the surface would need to be greater. To achieve a measurement on a more distant surface, a more powerful laser with a longer coherence length would be needed than what is available in current commercially available LDVs. Research into applying more powerful and temporally coherent lasers in LDVs is needed, and is outside the scope of this thesis.

In Figure 2.22, I demonstrate that by combining many signals, one can increase the ratio of seismic signal to speckle noise by nearly 30 dB. However, the performance of my algorithm varies depending on the specific attributes of the noise and signal. When evaluating speckle noise reduction, there are three primary factors to consider: the number of independent signals recorded, the velocity of the laser spot relative to the surface, and how different the seismic signal is from speckle noise. The more detectors used, the more coherent signal energy there is relative to the speckle noise. The lower the velocity of the laser spot relative to the surface, the lower the speckle noise is relative to the signal. The more separated the signal and noise are, in any domain, the better the signal energy can be separated from the noise energy. Thus, the smallest signal that can be recorded depends strongly on the specific acquisition scenario of the spacecraft. In the case of orbital asteroid seismology, we can consider improving the signal combining performance by designing a source with more distinct characteristics. A source instrument that vibrates the surface with a specific known frequency pattern, like a swept chirp, could possibly be more easily separated from speckle noise. Future studies should consider the design of asteroid seismic sources and choose specific sources that minimize overlap with speckle noise, if possible.

It is likely that continued development on a signal separation algorithm could increase the separation performance. I note three ways to potentially improve signal separation. First, one could take advantage of the correlation present in speckle noise. The noise at each time step is correlated with neighboring times. Instead of using a simple weighting matrix, which assumes independence, an estimation of the covariance could be used instead (Tarantola, 2005). Second, the signal separation basis or subspace could be chosen more optimally. In

my work, I explicitly define the subspace for separation; however, in the future, a general approach for finding the ideal subspace could be implemented using dictionary learning and machine learning approaches (Li et al., 2019). My framework also allows for the application of sparsity promoting solutions such as $l_1$-norm minimization instead of the conventional least squares approach (Davenport and Wakin, 2012). Thus, instead of imposing a sparse subspace upon the recorded signal, a future approach could be to find a domain where the signal is sparse, and then solve for the sparse representation without assuming any specific properties of the signal like a given bandwidth (Li et al., 2019). Lastly, one could improve recovery by solving a dual signal fitting model. By identifying a dictionary for the expected signal, and another dictionary for the expected speckle noise, one could solve for both simultaneously and yield a potentially better separation without making specific assumptions of the signal or noise (Li et al., 2019; Zhang et al., 2012).

In my acquisition scenario, I consider a laser with a wavelength of 775 nm. I choose this wavelength because it is common among commercially available laser systems with high power and long coherence lengths (aspects necessary for long distance acquisition). However, I have not made any claim about whether this is the optimal choice. Further research and development is needed to choose an optimal laser wavelength for orbital seismology. Additionally, the laser spot size influences speckle noise. In this study, I have chosen a spot size similar to what is achieved by commercially available systems (Dräbenstedt et al., 2012). Further research, involving an analysis of laser power, and detector sensitivity are necessary to determine whether this can be improved.

The asteroid 101955 Bennu has an estimated macro-porosity of over 60%, implying that there must be locations within 101599 Bennu that are either empty space or very sparsely filled with regolith (Scheeres et al., 2015). In my thesis, I assume that the void space corresponds to regions sparsely filled with regolith, such that the seismic waves may still propagate. If large spaces of vacuum were present within an asteroid, this could possibly present a challenge for seismic imaging, as seismic waves cannot travel through a vacuum.

In the future, numerical seismic imaging experiments could be conducted to test seismic imaging on asteroids with large void spaces.

Sava and Asphaug (2019) outline an approach to achieve full 3D coverage over time, but do not discuss how to generate a seismic source. In this thesis, I assume an impact source. If an impulsive impact source were used, then its repeatability will be limited by how many impactors can be carried within the spacecraft. Thus, alternative source methods may be desired. Natural sources are a possibility, but more research must be conducted to determine their magnitude, frequency, and whether they would be useful for imaging if their location is unknown. A landed vibrational source is also a possibility, and it could generate a wavelet of a specific nature, like a swept pulse. Whatever the case, when designing a source, or an acquisition scenario, it is important to consider the speckle noise, and how separated the speckle noise would be from the expected signal. The more separated they are, the better an LDV could record seismic data.

NASA actively seeks the development of new and innovative instrument concepts, but the path to spaceflight for new instruments is long and arduous. The work that I demonstrate in this thesis is theoretical. Although certain aspects have been tested by Dräbenstedt (2014) and Redding et al. (2016), a large portion of this work would benefit from laboratory testing. The next step is to design and test an LDV that implements the methods discussed in this thesis. Such work would boost the technology readiness level closer to the ultimate goal of a spaceflight ready instrument. Perhaps future researchers could one day use orbital seismic data to learn about asteroid and comet interiors, allowing us to understand the early history of our solar system and save the world from the next deadly asteroid.

REFERENCES CITED

A'Hearn, M. F., M. J. S. Belton, W. A. Delamere, J. Kissel, K. P. Klaasen, L. A. McFadden, K. J. Meech, H. J. Melosh, P. H. Schultz, J. M. Sunshine, P. C. Thomas, J. Veverka, D. K. Yeomans, M. W. Baca, I. Busko, C. J. Crockett, S. M. Collins, M. Desnoyer, C. A. Eberhardy, C. M. Ernst, T. L. Farnham, L. Feaga, O. Groussin, D. Hampton, S. I. Ipatov, J.-Y. Li, D. Lindler, C. M. Lisse, N. Mastrodemos, W. M. Owen, J. E. Richardson, D. D. Wellnitz, and R. L. White, 2005, Deep impact: Excavating comet Tempel 1: Science, **310**, 258–264.

Aki, K., and P. G. Richards, 2002, Quantitative Seismology, 2nd Ed.: University Science Books.

Asphaug, E., 2008, Critical crater diameter and asteroid impact seismology: Meteoritics & Planetary Science, **43**, 1075–1084.

———, 2009, Growth and evolution of asteroids: Annual Review of Earth and Planetary Sciences, **37**, 413–448.

Asphaug, E., M. Belton, D. Bockelee-Morvan, S. Chesley, M. Delbo, T. Farnham, Y. Gim, R. Grimm, A. Herique, W. Kofman, J. Oberst, R. Orosei, S. Piqueux, J. Plaut, M. Robinson, P. Sava, E. Heggy, W. Kurth, D. Scheeres, B. Denevi, E. Turtle, and P. Weissman, 2014, The Comet Radar Explorer Mission: AAS/Division for Planetary Sciences Meeting Abstracts #46, 209.07.

Asphaug, E., E. V. Ryan, and M. T. Zuber, 2002, Asteroid interiors, *in* Asteroids III: University of Arizona, Tuscon, 463–484.

Barnouin, O. S., et al., 2019, Shape of (101955) Bennu indicative of a rubble pile with internal stiffness: Nature Geoscience, **12**, 247–252.

Barucci, M. A., E. Dotto, and A. C. Levasseur-Regourd, 2011, Space missions to small bodies: asteroids and cometary nuclei: The Astronomy and Astrophysics Review, **19**, 48.

Benner, L. A. M., M. W. Busch, J. D. Giorgini, P. A. Taylor, and J.-L. Margot, 2015, Asteroid polarimetry, *in* Asteroids IV: University of Arizona, Tuscon, 151–164.

Binzel, R., et al., 2010, Earth encounters as the origin of fresh surfaces on near-earth asteroids: Nature, **463**, 331.

Castellini, P., G. Revel, and E. Tomasini, 1998, Laser Doppler vibrometry: a review of advances and applications: The Shock and vibration digest, **30**, 443–456.

Cheng, A., J. Atchison, B. Kantsiper, A. Rivkin, A. Stickle, C. Reed, A. Galvez, I. Carnelli, P. Michel, and S. Ulamec, 2015, Asteroid impact and deflection assessment mission: Acta Astronautica, **115**, 262 – 269.

Cheng, A., P. Michel, C. Reed, A. Galvez, I. Carnelli, and P. Headquarters, 2012, DART: Double asteroid redirection test: European Planetary Science Congress, 23–28.

Ciarletti, V., A. Herique, J. Lasue, A.-C. Levasseur-Regourd, D. Plettemeier, F. Lemmonier, C. Guiffaut, P. Pasquero, and W. Kofman, 2017, CONSERT constrains the internal structure of 67P at a few metres size scale: Monthly Notices of the Royal Astronomical Society, **469**, S805–S817.

Daly, M. G., O. S. Barnouin, C. Dickinson, J. Seabrook, C. L. Johnson, G. Cunningham, T. Haltigin, D. Gaudreau, C. Brunet, I. Aslam, A. Taylor, E. B. Bierhaus, W. Boynton, M. Nolan, and D. S. Lauretta, 2017, The OSIRIS-REx laser altimeter (OLA) investigation and instrument: Space Science Reviews, **212**, 899–924.

Davenport, M. A., and M. B. Wakin, 2012, Compressive sensing of analog signals using discrete prolate spheroidal sequences: Applied and Computational Harmonic Analysis, **33**, 438 – 472.

Delbo, M., M. Mueller, J. P. Emery, B. Rozitis, and M. T. Capria, 2015, Asteroid thermophysical modeling, *in* Asteroids IV: University of Arizona, Tuscon, 107–128.

Donges, A., and R. Noll, 2015, Laser Doppler methods, *in* Laser Measurement Technology: Springer, 11, 279–303.

Drabenstedt, A., 2007, Quantification of displacement and velocity noise in vibrometer measurements on transversely moving or rotating surfaces: Proc. SPIE, **6616**.

Dräbenstedt, A., 2014, Diversity combining in laser Doppler vibrometry for improved signal reliability: AIP Conf. Proc., **1600**, 263–273.

Dräbenstedt, A., J. Sauer, and C. Rembe, 2012, Remote-sensing vibrometry at 1550 nm wavelength: AIP Conference Proceedings, **1457**, 113–121.

Fomel, S., P. Sava, I. Vlad, Y. Liu, and V. Bashkardin, 2013, Madagascar: open-source software project for multidimensional data analysis and reproducible computational experiments: Journal of Open Research Software, **1**, e8.

Gault, D. E., 1963, The partition of energy for hypervelocity impact craters formed in rock: Proc. Sixth Hypervelocity Impact Symp., **2**, 419–456.

Grimm, R. E., D. E. Stillman, P. Sava, and D. Ittharat, 2015, Radio reflection imaging of asteroid and comet interiors II: Results and recommendations: Advances in Space Research, **55**, 2166 – 2176.

Güldemeister, N., and K. Wünnemann, 2017, Quantitative analysis of impact-induced seismic signals by numerical modeling: Icarus, **296**, 15–27.

Guo, G., S. Li, and Q. Tan, 2001, Statistical properties of laser speckles generated from far rough surfaces: International Journal of Infrared and Millimeter Waves, **22**, 1177–1191.

Hamm, M., M. Grott, E. Kührt, I. Pelivan, and J. Knollenberg, 2018, A method to derive surface thermophysical properties of asteroid (162173) Ryugu (1999JU3) from in-situ surface brightness temperature measurements: Planetary and Space Science, **159**, 1 – 10.

Heffels, A., M. Knapmeyer, J. Oberst, and I. Haase, 2017, Re-evaluation of Apollo 17 lunar seismic profiling experiment data: Planetary and Space Science, **135**, 43 – 54.

Herique, A., B. Agnus, E. Asphaug, A. Barucci, P. Beck, J. Bellerose, J. Biele, L. Bonal, P. Bousquet, L. Bruzzone, C. Buck, I. Carnelli, A. Cheng, V. Ciarletti, M. Delbo, J. Du, X. Du, C. Eyraud, W. Fa, J. G. Fernandez, O. Gassot, R. Granados-Alfaro, S. Green, B. Grieger, J. Grundmann, J. Grygorczuk, R. Hahnel, E. Heggy, T.-M. Ho, O. Karatekin, Y. Kasaba, T. Kobayashi, W. Kofman, C. Krause, A. Kumamoto, M. Küppers, M. Laabs, C. Lange, J. Lasue, A. Levasseur-Regourd, A. Mallet, P. Michel, S. Mottola, N. Murdoch, M. Mütze, J. Oberst, R. Orosei, D. Plettemeier, S. Rochat, R. RodriguezSuquet, Y. Rogez, P. Schaffer, C. Snodgrass, J.-C. Souyris, M. Tokarz, S. Ulamec, J.-E. Wahlund, and S. Zine, 2018, Direct observations of asteroid interior and regolith structure: Science measurement requirements: Advances in Space Research, **62**, 2141 – 2162. (Past, Present and Future of Small Body Science and Exploration).

Huebner, W. F., 2004, Seismological investigation of asteroid and comet interiors: Mitigation of hazardous comets and asteroids, 234.

Jenniskens, P., O. P. Popova, D. O. Glazachev, E. D. Podobnaya, and A. P. Kartashova, 2019, Tunguska eyewitness accounts, injuries, and casualties: Icarus, **327**, 4 – 18.

Jones, S., 2009, Elastic wave velocity, porosity, and pore geometry of ordinary chondrites and artificially shocked samples: Master's thesis, University of Calgary Department of Geosciences.

Kartashova, A., et al., 2018, Study of injuries from the Chelyabinsk airburst event: Planetary and Space Science, **160**, 107 – 114.

Kovach, R. L., and J. S. Watkins, 1973, The velocity structure of the lunar crust: The moon, **7**, 63–75.

Kueppers, M., I. Carnelli, A. Galvez, K. Mellab, P. Michel, A. Team, et al., 2015, The asteroid impact mission (AIM): Presented at the Proceedings of the European Planetary Science Congress, Nantes, France.

Landau, H. J., and H. O. Pollak, 1961, Prolate spheroidal wave functions, Fourier analysis and uncertainty – ii: Bell System Technical Journal, **40**, 65–84.

Lauretta, D. S., et al., 2019, The unexpected surface of asteroid (101955) Bennu: Nature, **568**, 55–60.

Li, C., Y. Zhang, and C. C. Mosher, 2019, A hybrid learning-based framework for seismic denoising: The Leading Edge, **38**, 542–549.

Lutzmann, P., B. Göhler, F. van Putten, and C. A. Hill, 2011, Laser vibration sensing: overview and applications: Electro-Optical Remote Sensing, Photonic Technologies, and Applications V, International Society for Optics and Photonics, SPIE, 11 – 26.

Massironi, M., et al., 2015, Two independent and primitive envelopes of the bilobate nucleus of comet 67P: Nature, **526**, 402.

Matsue, K., M. Yasui, M. Arakawa, and S. Hasegawa, 2019, Measurements of seismic waves induced by high-velocity impacts: Implications for seismic shaking surrounding impact craters on asteroids: Icarus, 113520.

Matter, A., M. Delbo, B. Carry, and S. Ligori, 2013, Evidence of a metal-rich surface for the asteroid (16) Psyche from interferometric observations in the thermal infrared: Icarus, **226**, 419 – 427.

Meschede, M. A., C. L. Myhrvold, and J. Tromp, 2011, Antipodal focusing of seismic waves due to large meteorite impacts on Earth: Geophysical Journal International, **187**, 529–537.

Moon, T., and W. Stirling, 2000, Signal spaces, *in* Mathematical Methods and Algorithms for Signal Processing: Prentice Hall, 2, 71–129.

Moore, H. J., G. V. Latham, and W. G. Mcdonald, 1970, Missile inpacts as sources of seismic energy on the Moon: Science, **168**, 242–244.

Morgan, S. P., and M. E. Ridgway, 2000, Polarization properties of light backscattered from a two layer scattering medium: Opt. Express, **7**, 395–402.

Nakamura, Y., and J. Koyama, 1982, Seismic Q of the lunar upper mantle: Journal of Geophysical Research: Solid Earth, **87**, 4855–4861.

Plescia, J. B., et al., 2018, APEX: asteroid probe experiment mission: Presented at the 49th Lunar and Planetary Science Conference Abstract #1999.

Quillen, A. C., Y. Zhao, Y. Chen, P. Sánchez, R. C. Nelson, and S. R. Schwartz, 2019, Impact excitation of a seismic pulse and vibrational normal modes on asteroid Bennu and associated slumping of regolith: Icarus, **319**, 312 – 333.

Redding, B., A. Davis, C. Kirkendall, and A. Dandridge, 2016, Measuring vibrational motion in the presence of speckle using off-axis holography: Appl. Opt., **55**, 1406–1411.

Rembe, C., et al., 2015, Speckle-insensitive laser-Doppler vibrometry with adaptive optics and signal diversity: AMA Conf. Proc., 505–510.

Renne, P. R., A. L. Deino, F. J. Hilgen, K. F. Kuiper, D. F. Mark, W. S. Mitchell, L. E. Morgan, R. Mundil, and J. Smit, 2013, Time scales of critical events around the cretaceous-paleogene boundary: Science, **339**, 684–687.

Richardson, J. E., H. J. Melosh, R. J. Greenberg, and D. P. O'Brien, 2005, The global effects of impact-induced seismic activity on fractured asteroid surface morphology: Icarus, **179**, 325 – 349.

Rothberg, S., M. Allen, P. Castellini, D. D. Maio, J. Dirckx, D. Ewins, B. Halkon, P. Muyshondt, N. Paone, T. Ryan, H. Steger, E. Tomasini, S. Vanlanduit, and J. Vignola, 2017, An international review of laser Doppler vibrometry: Making light work of vibration measurement: Optics and Lasers in Engineering, **99**, 11 – 22.

Rothberg, S., et al., 2004, Laser vibrometry meets laser speckle: Proc. SPIE, **5503**, 5503 – 5503 – 12.

Saiki, T., H. Sawada, C. Okamoto, H. Yano, Y. Takagi, Y. Akahoshi, and M. Yoshikawa, 2013, Small carry-on impactor of Hayabusa2 mission: Acta Astronautica, **84**, 227 – 236.

Sava, P., and E. Asphaug, 2018a, 3D radar wavefield migration of comet interiors: Advances in Space Research, **62**, 1146–1164.

———, 2018b, 3D radar wavefield tomography of comet interiors: Advances in Space Research, **61**, 2198–2213.

———, 2019, Seismology on small planetary bodies by orbital laser Doppler vibrometry: Advances in Space Research, **64**, 527 – 544.

Sava, P., D. Ittharat, R. Grimm, and D. Stillman, 2015, Radio reflection imaging of asteroid and comet interiors I: Acquisition and imaging theory: Advances in Space Research, **55**, 2149 – 2165.

Scheeres, D. J., D. Britt, B. Carry, and K. A. Holsapple, 2015, Asteroid interiors and morphology, *in* Asteroids IV: University of Arizona, Tuscon, 745–766.

Slepian, D., and H. O. Pollak, 1961, Prolate spheroidal wave functions, Fourier analysis and uncertainty – i: Bell System Technical Journal, **40**, 43–63.

Staszewski, W. J., R. bin Jenal, A. Klepka, M. Szwedo, and T. Uhl, 2012, A review of laser Doppler vibrometry for structural health monitoring applications: Structural Health Monitoring II, Trans Tech Publications Ltd, 1–15.

Syal, M. B., J. M. Owen, and P. L. Miller, 2016, Deflection by kinetic impact: Sensitivity to asteroid properties: Icarus, **269**, 50 – 61.

Tarantola, A., 2005, The least-squares criterion, *in* Inverse Problem Theory and Methods for Model Parameter Estimation: SIAM, 3, 57–80.

Thompson, A. R., J. M. Moran, and G. W. Swenson, 2017, *in* Van Cittert–Zernike Theorem, Spatial Coherence, and Scattering: Springer International Publishing, 767–786.

Titley, S. R., 1966, Seismic energy as an agent of morphologic modification on the moon: U.S. Geol. Survey, Astrogeologic Studies, Ann. Prog. Repr. pt. A, 87–101.

Tonry, J. L., L. Denneau, A. N. Heinze, B. Stalder, K. W. Smith, S. J. Smartt, C. W. Stubbs, H. J. Weiland, and A. Rest, 2018, ATLAS: A high-cadence all-sky survey system: Publications of the Astronomical Society of the Pacific, **130**, 064505.

Walker, J. D., E. J. Sagebiel, and W. F. Huebner, 2006, A preliminary analysis of seismological techniques to study Eros and other asteroids: Advances in Space Research, **37**, 142 – 152.

Watanabe, S., M. Hirabayashi, N. Hirata, N. Hirata, R. Noguchi, Y. Shimaki, H. Ikeda, E. Tatsumi, M. Yoshikawa, S. Kikuchi, H. Yabuta, T. Nakamura, S. Tachibana, Y. Ishihara, T. Morota, K. Kitazato, N. Sakatani, K. Matsumoto, K. Wada, H. Senshu, C. Honda, T. Michikami, H. Takeuchi, T. Kouyama, R. Honda, S. Kameda, T. Fuse, H. Miyamoto, G. Komatsu, S. Sugita, T. Okada, N. Namiki, M. Arakawa, M. Ishiguro, M. Abe, R. Gaskell, E. Palmer, O. S. Barnouin, P. Michel, A. S. French, J. W. McMahon, D. J. Scheeres, P. A. Abell, Y. Yamamoto, S. Tanaka, K. Shirai, M. Matsuoka, M. Yamada, Y. Yokota, H. Suzuki, K. Yoshioka, Y. Cho, S. Tanaka, N. Nishikawa, T. Sugiyama, H. Kikuchi, R. Hemmi, T. Yamaguchi, N. Ogawa, G. Ono, Y. Mimasu, K. Yoshikawa, T. Takahashi, Y. Takei, A. Fujii, C. Hirose, T. Iwata, M. Hayakawa, S. Hosoda, O. Mori, H. Sawada, T. Shimada, S. Soldini, H. Yano, R. Tsukizaki, M. Ozaki, Y. Iijima, K. Ogawa, M. Fujimoto, T.-M. Ho, A. Moussi, R. Jaumann, J.-P. Bibring, C. Krause, F. Terui, T. Saiki, S. Nakazawa, and Y. Tsuda, 2019, Hayabusa2 arrives at the carbonaceous asteroid 162173 Ryugu—a spinning top–shaped rubble pile: Science, **364**, 268–272.

Yoshikawa, M., J. Kawaguchi, and A. Fujiwara, 2015, Hayabusa sample return mission, *in* Asteroids IV: University of Arizona, Tuscon, 397–418.

Zhang, J., C. Zhao, R. Xiong, S. Ma, and D. Zhao, 2012, Image super-resolution via dual-dictionary learning and sparse representation: 2012 IEEE International Symposium on Circuits and Systems (ISCAS), 1688–1691.